Revision 1:

Experimental calibration of an Fe^{3+}/Fe^{2+}-in-amphibole oxybarometer and its application to shallow magmatic processes at Shiveluch Volcano, Kamchatka

Word Count: 8910

Authors: Andrea E. Goltz[1], Michael J. Krawczynski[1], Molly C. McCanta[2], M. Darby Dyar[3,4]

Affiliations: (1) Department of Earth and Planetary Sciences, Washington University in St. Louis, 1 Brookings Drive, St. Louis, MO, 63130 **(2)** Department of Earth and Planetary Sciences, University of Tennessee at Knoxville, 1621 Cumberland Avenue, Knoxville, TN, 37996 **(3)** Department of Astronomy, Mount Holyoke College, 50 College Street, South Hadley, MA, 01075 **(4)** Planetary Science Institute, 1700 East Fort Lowell, Suite 106, Tucson, AZ, 85719

Abstract

Oxygen fugacity is an important but difficult parameter to constrain for primitive arc magmas. In this study, the partitioning behavior of Fe^{3+}/Fe^{2+} between amphibole and glass synthesized in piston cylinder and cold-seal apparatus experiments is developed as an oxybarometer, applicable to magmas ranging from basaltic to dacitic composition. The partitioning of Fe^{2+} is strongly dependent on melt polymerization; the relative compatibility of Fe^{2+} decreases with increasing polymerization. The Fe^{2+}/Mg distribution coefficient between amphibole and melt is a relatively constant value across all compositions, and is on average 0.27. The amphibole oxybarometer is

applied to amphibole in mafic enclaves, cumulates, and a basaltic tephra erupted from Shiveluch volcano in Kamchatka with measured Fe^{3+}/Fe_{Total}. An average Fe^{3+}/Fe^{2+} amphibole-glass distribution coefficient for basalt is used to convert the Fe^{3+}/Fe_{Total} of amphibole in samples from Shiveluch to magmatic oxygen fugacity relative to NNO. The f_{O2} of primitive melts at the volcano is approximately NNO+2 and is faithfully recorded in amphibole from an amphibole-rich cumulate and the basaltic tephra. Apparently higher f_{O2} recorded by amphibole in mafic enclaves likely results from partial dehydrogenation of amphibole during residence in a shallow andesite storage region. We identify three pulses of mafic magma recharge within two weeks of, a month before, and two to three months before eruption, and find that, at each of these times, the host andesite was recharged by at least two magmas at varying stages of differentiation. Application of the amphibole oxybarometer not only gives insight to magmatic f_{O2} but also potentially details of shallow magmatic processes.

Keywords: Amphibole, Oxybarometer, Subduction zones, XAFS, Experimental petrology

Introduction

Oxygen fugacity is a key intrinsic parameter for magma genesis. Magmatic oxygen fugacity effects mineral stability, which, in turn, influences magmatic differentiation (e.g., Osborn, 1959; Hamilton et al., 1964) and the formation of porphyry deposits worldwide (e.g., Mungall, 2002; Core et al., 2006; Richards, 2011; Lee et al., 2012; Sun *et al*., 2013). The oxygen fugacity of primitive magmas is also of interest because it is thought to be reflective of the oxygen fugacity of mantle sources (e.g., Ballhaus et al., 1990; Carmichael, 1991; Cottrell and

Kelley, 2013; Grocke et al., 2016) or pressure, temperature, and degree of melting (e.g., Rowe et al., 2009; Gaetani, 2016).

Oxygen fugacity is particularly difficult to estimate for primitive arc magmas. The oxygen fugacity of a melt is most commonly estimated using two-oxide oxybarometry (Buddington and Lindsley, 1964), but two-oxide pairs are rare or absent in some natural samples and subject to re-equilibration during cooling (e.g., Hou et al., 2020). Researchers have tried to probe the oxygen fugacity of primitive melts by analyzing olivine-hosted melt inclusions using X-Ray Absorption Near Edge Structure (XANES; e.g., Kelley and Cottrell, 2009; Brounce et al., 2014) and by analyzing their S-speciation (e.g., Rowe et al., 2009). However, because of rapid H diffusion through olivine, the oxygen fugacity determined from a melt inclusion may not reflect the pre-entrapment oxygen fugacity of a primitive melt (Bucholz et al., 2013). Crustal processing such as crustal assimilation and syn-eruptive oxidation may further convolute the oxygen fugacity of primitive melts and make measurements of oxygen fugacity from any of the above methods difficult to interpret as a signature of primitive melt oxygen fugacity (e.g., Mathez, 1984; Ague and Brimhall, 1988; Lee et al., 2005).

Amphibole is a desirable target for development of an alternative oxybarometer in arc systems. It is a hydrous mineral commonly found as a phenocryst in andesite, dacite, and rhyolite melts and less commonly in hydrous basalts (e.g., Martin, 2007; references therein). It is also a common mineral in cumulates found at arc settings and in suprasubduction zone ophiolites (e.g., Arculus and Wills, 1980; Beard, 1986; Parlak et al., 2000; Greene et al., 2006; Coltori et al., 2007; Jagoutz et al., 2011). Importantly for its development as a single-mineral oxybarometer, Fe^{3+} and Fe^{2+} are both compatible in amphibole's octahedral sites (i.e., $D \geq 1$ for at least one octahedral site; e.g., Dalpé and Baker, 2000). A previous experimental study (King et al., 2000)

found that Fe^{3+} partitioning into amphibole has a strong dependence on melt oxygen fugacity, and kept pressure, temperature, and composition constant. In this contribution, we calibrate the Fe^{3+}/Fe^{2+} of igneous amphibole as an indicator of magmatic oxygen fugacity at arc settings using experimentally determined amphibole-melt partition coefficients at a wide range of pressures, temperatures, and compositions applicable to arc settings. We then apply our oxybarometer to amphibole in cumulate, tephra, and mafic enclave samples collected from Shiveluch Volcano, Kamchatka, and, using the samples' previously reported whole rock chemistries and petrography, interpret the primitive oxygen fugacity of this volcano to be ~NNO+2. Insight on the volcano's plumbing system is also gained by calculating and comparing the variable residence time of amphiboles in several mafic enclaves.

Methods

Starting Material

Experiments were conducted on five different synthetic bulk compositions: four basaltic and one andesitic (**Table 1**). Two of the basaltic compositions are equivalent to the major element composition of tephra erupted at Shiveluch volcano 3600 BP and 7600 BP (e.g., Volynets et al., 1997; Ponomareva et al., 2007) and differ predominately in their potassium contents. The other two basaltic compositions are calculated parental magmas to the tephra compositions. The parental composition of the 3600 BP tephra was calculated by Gavrilenko et al. (2016) by adding olivine back to the original tephra composition with a variable K_D until it reached equilibrium with Fo_{90} olivine. The parental composition of the 7600 BP tephra was calculated by iterative addition of olivine in 1 wt % steps assuming a K_D=0.32 and all iron as Fe^{2+}, until it reached

equilibrium with olivine of Fo_{90}. The andesitic composition is the Soufriere Hills dome sample MVO34 (Barclay et al., 1998).

Synthetic mixes were made by combination of simple oxides, carbonates (Na_2CO_3, K_2CO_3), hydroxides ($Mg(OH)_2$), and silicates ($CaSiO_3$). Iron was added to the mixes using both Fe_2O_3 and Fe^0 sponge in equal molar proportions. The Fe^0 sponge was added to the mixes after an initial homogenization step using a silicon-nitride ball mill filled with isopropanol. The mix, including the Fe^0 sponge, was gently ground by hand in an agate mortar until enough isopropanol had evaporated so that the metal particles would not separate by density. Material used in high-pressure experiments was pre-conditioned at the nickel-nickel oxide buffer (NNO) by suspending the mix (bound with polyvinyl alcohol) on a thin (0.2 mm diameter) Pt wire in a CO_2-H_2 Deltech gas mixing furnace at 1000°C for ~24 hours.

Experimental Procedures

All experiments were run using piston cylinder apparatuses at Washington University in St. Louis. Two experimental assemblies were used depending on the pressure of the experiments. For 500 MPa experiments, an assembly with a 19.1 mm outer diameter with NaCl pressure medium, Pyrex-glass inner sleeve, and graphite furnace was used. Experiments at 1 GPa an assembly with a 12.5 mm outer diameter, with a thin piece of Pb-foil around the outside for lubrication, $BaCO_3$ as the pressure medium and a graphite furnace (**Figure 1a**). Experiments were first pressurized to the target experimental pressure and then heated at 50°C/min to 865°C for a dwell of 6 minutes and then heated at the same rate to the target temperature. Temperature was monitored using a Type C thermocouple and controlled within 5 degrees of the target temperature using a Eurotherm PID controller. Experiments were quenched by turning off the

power while maintaining experimental pressure (isobaric quench). Run times for all experiments were ~48 hours (**Table 2**).

All experiments run at NNO used a triple capsule design (**Figure 1b**). Twenty milligrams of a 5:1 mixture of Ni:NiO was packed in a Pt capsule with 2-3 μL of deionized water, the capsule was then crimped and welded shut using a TIG welder cooled under Argon gas. A gold sample capsule welded and flattened on one end was packed with 30 mg of sample and 6 μL of deionized water for water saturated runs or 2 μL for water undersaturated runs, and was then crimped, welded shut, and flattened. Both the sample and the buffer capsules were packed in a larger diameter outer Au capsule flattened and welded on one end. In addition to the Au sample and Pt buffer capsules, the outer Au capsule contained 20 μL of deionized water for water saturated runs or 2 μL for water undersaturated experiments and powdered Al_2O_3. The powdered alumina made the sample extraction process after the experiment easier because the three capsules did not pressure weld together. The outer capsule was then crimped, welded, and flattened.

Experiments run at the ruthenium-ruthenium oxide buffer (Ru-RuO_2) used a single capsule design based on that described in Zhang et al. (2018) (**Figure 1c**). The Ru-RuO_2 buffer is a relatively oxidizing buffer at high pressures (close to magnetite-hematite; O'Neill and Nell, 1997). Neither ruthenium nor ruthenium oxide reacts with or is soluble in silicate melts meaning that the buffer can be in direct contact with the sample, thus obviating the need for water saturation to buffer experiments at this oxygen fugacity. In the single capsule design, water and sample were sandwiched between two layers of buffer in a gold capsule, which was then crimped, welded, and flattened.

Water loss from the capsule during welding was monitored by weighing before and after welding; in all cases, water loss was within the analytical uncertainty of the balance (0.1 mg). The capsule's seal was evaluated by weighing before and after heating in a 300°F oven for 1-2 minutes. If weight loss was ≥0.5 mg, the capsule was reinspected, rewelded, reweighed, and reheated to check for an improvement in the seal. The total loss of water from the capsule was never greater than 2 mg (i.e., 2 μL). The presence of water in the capsule after the experiment was assessed by drilling a small hole into the capsule, releasing free water. The presence of the buffering assemblage (Ni-NiO or Ru-RuO_2) was also confirmed at the end of the experimental run by inspection of the platinum capsule (Ni-NiO) or by inspection in thin section using back-scattered electron microscopy (BSE).

Analytical Methods

Electron Probe Microanalysis (EPMA). Microprobe analysis of natural and synthetic amphibole was performed on a JEOL JXA-8200 electron microprobe equipped with five wavelength-dispersive spectrometers. Analyses were acquired using the Probe for EPMA software (Donovan et al., 2012); background correction was performed using a Mean Atomic Number (MAN) correction (Donovan and Tingle, 1996); and corrections for atomic number, X-ray absorption, and secondary fluorescence (ZAF) were performed using the CITZAF software (Armstrong et al., 2013). Analytical conditions for sample analyses were: 15 kV accelerating potential, 1-3 μm beam diameter for minerals and 10-30 μm for glasses, and 25 nA beam current.

The instrument was standardized for the analysis of Si, Ti, Mg, Al, Mn, Fe, Cr, Ni, Ca, Na, and K before the run using natural primary standards Amelia albite, Gates wollastonite, Elba hematite, Madagascar orthoclase, Durango apatite, and pyrite and synthetic forsterite, Mn-

olivine, Ni-olivine, chromite, and rutile. Other secondary standards were used for the MAN correction (e.g., Donovan et al., 2012). Na and K were analyzed in the first 20 (for K) to 45 (for Na) seconds using TAP and PETJ crystals, respectively, to mitigate the effects of alkali migration during analysis. For analyses of glass with beam sizes <10 μm, a 10 nA beam current was used and a time dependent intensity analysis (TDI) procedure was applied to determine the concentrations of Na and Si in the glass before beam damage. The TDI correction mitigates the effect of beam damage on Na and Si migration by using a linear regression fit to the log intensity of the element versus time at 9-second intervals to determine the log intensity (and, by extension, concentration) initially. The accuracy of the standardization was verified by periodic analyses of the secondary standard Kakanui hornblende throughout the analytical session.

X-Ray Absorption Fine Structure. Samples were analyzed over the course of two sessions at beamline 13-IDE at the Advanced Photon Source at Argonne National Lab and one session at Beamline 4-BM at the National Synchrotron Light Source II at Brookhaven National Lab. The spectra of the Fe K-edge spectra were scanned from 7012-7356 eV in fluorescence mode. From 7012-7100 eV, the resolution was 2.5 eV; from 7100-7142 (which includes the pre-edge and main absorption peak energies), a higher resolution of 0.1 eV was used; from 7142-7160, the resolution was 2 eV; and from 7160-7356, the resolution was 3 eV. The beam was focused to a 3-5 μm diameter using Kirkpatrick-Baez mirrors.

Amphibole was analyzed in-situ in thin section for all analyses. The orientation of amphibole affects the spectral intensity and shape of X-Ray Absorption Fine Structure (XAFS) spectra because of its anisotropy (e.g., Delaney et al., 1996; Dyar et al., 2016). To account for the unknown crystallographic orientation of analyzed grains in this study, the Fe^{3+}/Fe_{Total} of amphibole was determined using partial least squares, a multivariate regression technique, using

the Data Exploration, Visualization, and Analysis for Spectroscopy (DEVAS) website at nemo.mtholyoke.edu (Carey et al., 2017). A predictive model using 186 spectra of oriented and unoriented amphibole Fe^{3+}/Fe_{Total} standards from a previous study (Dyar et al., 2016) was generated using the least absolute shrinkage and selection operator (Lasso). Spectra were pre-processed by normalizing intensities to 1 at 7350 eV and by applying a Kajfosz-Kiwiatek baseline correction (bottom width=100, top width=26; Kajfosz and Kwiatek, 1987). The model was cross-validated for 14 folds. The model with the lowest mean squared error (α=0.0001319 for this model) was used to predict unknown amphibole Fe^{3+}/Fe_{Total}. The root mean square error of cross validation (RMSE-CV) of this model is taken as the accuracy of the predictions of Fe^{3+}/Fe_{Total} of amphibole unknowns; in our model, the RMSE-CV was ±10.8. The root mean square error of calibration (RMSE-C, describing the model's ability to reproduce the Fe^{3+}/Fe_{Total} of standards) of this model was ±4.7 (R^2=0.963). See Dyar and Ytsma (2021) for more information on these accuracy measures.

Results

Experimental Observations and Evidence of Equilibrium

Phase relations and average phase compositions in our experiments are reported in **Tables 2 and 3**, respectively. Phase proportions were calculated by mass balance using starting compositions, average phase compositions, and the mass balance program LIME (Krawczynski and Olive, 2011; Prissel et al., in prep). The mass balance calculations show that experimental run products are deficient in Na_2O compared to the bulk starting material. In some cases, this deficit is as high as 77% of the total Na_2O. Because the experiments were run at fluid-saturated

This is the peer-reviewed, final accepted version for American Mineralogist, published by the Mineralogical Society of America.
The published version is subject to change. Cite as Authors (Year) Title. American Mineralogist, in press.
DOI: https://doi.org/10.2138/am-2022-8031. http://www.minsocam.org/

conditions, and a fluid phase would preferentially scavenge sodium, we believe that the unaccounted for sodium was dissolved in this phase. Another possibility to explain the low Na_2O concentrations in the synthetic minerals and glass is sodium migration during EPMA analysis. This effect would be most pronounced in high sodium glass and plagioclase, and our hydrous glasses are sensitive to electron beam damage. While this possibility cannot be discounted as contributing to apparent sodium loss, it is not likely the sole factor controlling the sodium deficit in experimental phases, since our analytical conditions (large beam diameter, and TDI corrections) were chosen to minimize the effects of sodium migration.

Water contents of glasses in water-saturated experiments were calculated using the equations of Papale et al. (2006), assuming XH_2O in the fluid phase was equal to 1. For 1 GPa experiments, the water content was calculated to be 17-20 wt% and for 0.5 GPa experiments, the water content calculated to be about 10 wt% (**Table 2**). The water content of water-undersaturated experiments was calculated using the percent glass and the amount of water added to the capsule at the start of the experiment. As a result of the high water contents (which far exceed the "quenchability limit" of glass found by Gavrilenko et al., 2019), experimental glass is vesicular and frothy (**Figure 2**). The quenchability limit of glass is 9±1 wt% in basaltic glasses, which is consistent with low EPMA analytical totals in our experimental glasses (**Table 3**), and the frothy and vesicular nature of the glass may also contribute to low EPMA totals. Especially for water saturated experiments with experimental water contents significantly greater than 9 wt%, the deficit from 100 wt% of these totals cannot be interpreted as the water content of the melt.

Amphibole and glass are the two most abundant phases in most experiments. At higher temperatures, olivine and pyroxene are also stable. Due to the high water content of the

experiments, plagioclase was not a major crystallizing phase in experiments at 1 GPa, but was present in three experiments run on andesite starting compositions. Two of the three—F177 and F176—were run at 0.5 GPa (**Table 2**); the lower water content of these experiments may have allowed plagioclase to crystallize closer to the liquidus. The third experiment was run at a relatively low temperature and was buffered at relatively high f_{O2} (an experiment run at intermediate f_{O2} at the same pressure and temperature conditions did not have equilibrium plagioclase). Plagioclase has been shown to crystallize at higher temperatures at more oxidizing conditions (e.g., Hamilton et al., 1964), which would explain its presence in the higher f_{O2} experiment.

Attainment of equilibrium in these experiments is suggested by crystal morphology, homogeneous crystal chemistry, and Fe/Mg equilibrium partitioning ratios for olivine and pyroxene. Silicate crystal size varies from ~5 μm to >100 μm (although smaller crystals were more common; **Figure 2**). Crystals are euhedral and unzoned. Coupled with the relatively low standard deviation between glass analyses within a single experiment (**Table 3**), the geochemical data suggests equilibrium growth. The Fe/Mg distribution coefficients for olivine and clinopyroxene (all calculated assuming all iron as ferrous) from experiments buffered at NNO are 0.26-0.35 for olivine and 0.21-0.22 for clinopyroxene, which is within uncertainty of what is to be expected from other studies (Sisson and Grove, 1993; Sugawara, 2000; Kushiro and Mysen, 2002; Putirka, 2008; Bédard, 2010), and would also suggest growth at equilibrium conditions.

Summary of Synthetic Amphibole and Glass Major Element Compositions

In addition to analyzing amphibole and glass in our piston cylinder experiments conducted on basaltic and andesitic compositions, we also analyzed amphiboles from experiments previously reported in McCanta et al. (2007), conducted on a dacitic starting composition at lower pressures (<500 MPa) using a cold-seal Waspaloy pressure vessel or an internally heated pressure vessel and an oxygen fugacity of NNO+1. All amphiboles in our experiments are solid solutions between tschermakite and pargasite end-members on the basis of their major element compositions and the classification scheme of Leake et al. (1997, 2003). The amphiboles are calcic, with ≥1.5 PFU calcium in the B site and are dominantly magnesian with $Mg/(Mg+Fe^{2+})>0.5$. Si PFU varies from 6.2 to 6.6 and the A site occupancy by sodium and potassium ranges from 0 to 0.78. There is no discernable trend in Al, Ca, Ti, or Na with decreasing Mg PFU in amphibole, but experiments run at the Ru-RuO_2 buffer tend to be relatively lower in Ti and Na (**Figure 3**). Glass in our experiments is basaltic andesite to dacite in composition when normalized to 100 wt% on an anhydrous basis.

Fe^{3+} and Fe^{2+} partitioning in amphibole

Fe^{3+} and Fe^{2+} amphibole-melt partition coefficients were determined using our XAFS analyses of amphibole and calculated Fe^{3+}/Fe^{2+} ratios of glasses. For amphibole, the Fe^{3+}/Fe_{Total} determined by XAFS analysis (as described in the methods section) and total molar iron from EPMA were used to determine Fe^{3+} and Fe^{2+}. We did not measure the Fe^{3+}/Fe^{2+} ratio of coexisting glass in these experiments and instead calculated them using equation 7 of Kress and Carmichael (1991). Other studies (e.g., Sisson and Grove, 1993; Moore et al., 1995; King et al., 2000; Gaillard et al., 2001; Wilke et al., 2002; Botcharnikov et al., 2005; Zhang et al., 2016) have shown good agreement between measured Fe^{3+}/Fe^{2+} of glass and calculated values for both

hydrous and anhydrous glasses. Additionally, due to their very high water contents, glasses in our experiments are more prone to oxidation during measurement by XAFS, and, as an effect, reliable, direct measurements of them are more difficult (Cottrell et al., 2018; Blundy et al., 2020). It is notable that two glasses with > 8wt% H_2O analyzed by Blundy et al. (2020) using XAFS did not have measured Fe^{3+}/Fe_{Total} equal to the predicted Fe^{3+}/Fe_{Total} value from the equation of Kress and Carmichael (1991). However, Blundy et al. (2020) did not find systematic changes in Fe^{3+}/Fe_{Total} with water content, and the two data points cannot be interpreted as conclusive evidence that the Kress and Carmichael (1991) equation is not applicable to glasses with very high water content. For each experiment, the Fe^{3+} and Fe^{2+} of melt in equilibrium with amphibole were calculated using the composition of the equilibrium glass, experimental pressure and temperature, and experimental oxygen fugacity from the equations of O'Neill and Pownceby (1993) for NNO and O'Neill and Nell (1997) for Ru-RuO_2.

Partition coefficients of Fe^{3+}, Fe^{2+}, Mg, and Fe^{2+}/Mg for each experiment are presented in **Table 4** and a summary of average partition coefficients correlated with oxygen fugacity and starting composition is found in **Table 5**. The amphibole-melt Fe^{3+} partition coefficient (D^{Fe3+}) does not vary with temperature, pressure, or melt composition (quantified as non-bridging oxygen (NBO) divided by tetrahedrally coordinated cations (T); Mysen, 1988), but, on average, experiments run at the Ru-RuO_2 buffer (i.e., high oxygen fugacity) have a higher D^{Fe3+} than experiments run at NNO or NNO+1. This is consistent with behavior described in King et al. (2000), who noted a difference between the partitioning of Fe^{3+}/Fe_{Total} at high oxygen fugacities and oxygen fugacity near NNO (**Figures 4, 5, 6**). Not including experiments run at Ru-RuO_2, the average D^{Fe3+} for all starting compositions is 2.66 ±0.57 (2 times standard error, 2SE); for high f_{O2} experiments it is 3.88 ±0.51.

This is the peer-reviewed, final accepted version for American Mineralogist, published by the Mineralogical Society of America.
The published version is subject to change. Cite as Authors (Year) Title. American Mineralogist, in press.
DOI: https://doi.org/10.2138/am-2022-8031. http://www.minsocam.org/

297 The amphibole-melt Fe^{2+} and Mg partition coefficients (D^{Fe2+} and D^{Mg}) have a strong
298 dependence on the structure, and by extension composition, of silicate melt but no correlation
299 with pressure, water content, or oxygen fugacity (**Figures 4-6**). Both partition coefficients
300 increase with decreasing NBO/T. On average, for basalt at intermediate f_{O2} (i.e., NNO and
301 NNO+1), D^{Fe2+} is 1.18 ±0.20; for andesites it is 2.34 ±0.55; and for dacites it is 5.53 ±1.24
302 (quoted error is 2SE; **Table 5**). D^{Fe2+} has a weak dependence on temperature for experiments run
303 on andesitic and dacitic starting compositions. The amphibole-melt Fe^{2+}/Mg distribution
304 coefficient ($K^{Fe2+/Mg}$, defined as D^{Fe2+}/D^{Mg}) is independent of melt structure and has an average
305 value across all experiments at intermediate f_{O2} of 0.27 ±0.02 (2SE).
306 The amphibole-melt distribution coefficient of the ferric ferrous ratio was also calculated
307 from our data. We define this term, $K^{Fe3+/Fe2+}$, as:
308

$$K^{Fe3+}/_{Fe2+} = \frac{\left(\frac{Fe^{3+}}{Fe^{2+}}\right)_{amph}}{\left(\frac{Fe^{3+}}{Fe^{2+}}\right)_{melt}}$$

309
310 We apply this ratio to determine the oxygen fugacity of natural samples from the ferric-ferrous
311 ratio of amphibole because it is independent of the melt's total iron content. We exclude
312 experiments run at the Ru-RuO_2 buffer from this calibration because the oxygen fugacity of
313 those experiments is significantly higher than would be expected for natural arc magmas. On
314 average, $K^{Fe3+/Fe2+}$ of basalts, andesites, and dacites at intermediate f_{O2} (i.e., NNO-NNO+1) are
315 2.02 ±0.31, 0.96 ±0.14, and 0.62 ±0.15, respectively (**Figure 6, Table 5**).
316
317 **XAFS Measurements of Amphiboles in Natural Samples**

Natural samples in which amphibole was analyzed were all erupted from Shiveluch Volcano in the Kamchatkan arc. For full descriptions of samples besides the 3600 BP tephra, the reader is directed to Goltz et al. (2020); descriptions of the tephra may be found in Volynets et al. (1997) and Ponomareva et al. (2007). To summarize, all but samples 04L, 16B, and the 3600 BP tephra are amphibole and olivine-phyric quenched liquid cognate xenoliths (mafic enclaves) with basaltic to basaltic andesite bulk compositions that were erupted in pyroclastic flows mostly composed of andesite. Samples 04L and 16B are clinopyroxene and amphibole-rich cumulates. The 3600 BP tephra is one of two basaltic tephra erupted from Shiveluch and contains amphibole and phlogopite phenocrysts. The composition of this tephra has been hypothesized to be representative of a magmatic composition parental to the less magnesian mafic enclaves (e.g., Volynets et al., 1997; Goltz et al., 2020). Both the tephra and mafic enclaves show evidence for co-existence of high Mg# amphibole (i.e., Mg#>74) and high forsterite olivine (i.e., Fo_{90-92}), which implies crystallization from a super-hydrous primary magma, with an estimated primary magmatic water content ranging up to 10 wt% H_2O. Magmas at Shiveluch are primarily products of flux melting of the mantle overlying the subducting Pacific plate. Other possible contributions to primary magmas at Shiveluch include melting of a hydrous pyroxenite upper mantle layer (KUMA; Nikulin et al., 2010; Nikulin et al., 2012), slab melting caused by an underlying slab tear (e.g., Peyton et al., 2001; Yogodzinski et al., 2001; Park et al., 2002; Levin et al., 2002; Jiang et al., 2009), and melting of the subducting Emperor Seamounts (e.g., Nishizawa et al., 2017).

Amphibole in the enclaves spans a relatively wide range of Fe^{3+}/Fe_{Total}, from 16.7% to 84.1% (excluding statistical outliers; **Table 6**). The Fe^{3+}/Fe^{2+} of amphibole analyzed in natural samples is summarized by sample in **Figure 7**. The summarized dataset excludes analyses from

This is the peer-reviewed, final accepted version for American Mineralogist, published by the Mineralogical Society of America.
The published version is subject to change. Cite as Authors (Year) Title. American Mineralogist, in press.
DOI: https://doi.org/10.2138/am-2022-8031. http://www.minsocam.org/

within 500 microns of amphiboles that were highly oxidized (i.e., predicted Fe^{3+}/Fe_{Total}>90%). Highly oxidized amphiboles were observed in three contexts within our samples: the oxidized andesite surrounding the mafic enclaves, the contact between the enclave or cumulate and the andesite, and a single isolated grain in the tephra. The Fe^{3+}/Fe^{2+} ratio of these amphiboles are not representative of magmatic oxidation states and most likely reflect post-crystallization oxidation during eruption or magma mixing. Excluded analyses and images may be found in the supplementary data, but further discussion of these analyses is beyond the scope of this contribution.

Because amphiboles in these natural samples are commonly zoned in major elements (i.e., Mg#, Al_2O_3), we investigated the possibility of zoning in Fe^{3+}/ Fe_{Total} by analyzing multiple points in single grains. The criterion for statistically significant zoning is an intracrystalline compositional variation greater than twice the accuracy of the model used to determine amphibole Fe^{3+}/Fe_{Total} ($\sigma\approx11$, see Methods). Only 8 crystals of >69 analyzed grains met this criterion. Zoning in these grains is irregular and is not continuous from core to rim. Neither amphibole Mg# nor Al_2O_3 correlates with Fe^{3+}/Fe_{Total} in these grains. Because of the irregularity of the zoning profiles, the lack of correlation with other elements, and that often one analysis point in each of these crystals is responsible for their qualification as zoned, we take these zoned crystals to be outliers in our larger dataset.

Discussion

Fe^{3+} partitioning between amphibole and melt

Results from our experiments show that Fe^{3+} is compatible in amphibole (i.e., D^{Fe3+}>1). This result is consistent with predictions from lattice strain models (e.g., Dalpé and Baker, 2000;

Adam et al., 2007), partitioning data from King et al. (2000), and the wide range of Fe^{3+} observed in naturally occurring amphiboles (Dyar et al., 1992, 1993). The partitioning of Fe^{3+} between amphibole and melt is not affected by pressure, temperature, or melt composition; however, experiments buffered at high f_{O2} (Ru-RuO_2) have a higher D^{Fe3+} than experiments buffered at intermediate f_{O2} (NNO or NNO+1), on average (3.9 vs. 2.7). A similar relationship between f_{O2} and Fe^{3+} partitioning between amphibole and melt was reported by King et al. (2000). The difference in D^{Fe3+} between experiments at different f_{O2} might be an effect of changing Fe^{3+} behavior in the melt with changing oxygen fugacity. In their study of andesitic glass at variable f_{O2}, Zhang et al. (2016) showed that Fe^{3+} became more network-modifying as its concentration increased (i.e., at higher f_{O2}). The change in the behavior of Fe^{3+} in the melt may lead to the observed difference in its partitioning behavior.

The lower Na and Ti content of amphibole synthesized at high f_{O2} relative to amphibole at lower f_{O2} suggests a different substitution mechanism to accommodate the high relative amount of Fe^{3+} in amphibole at these conditions. The low Na content of some amphiboles synthesized at the Ru-RuO_2 buffer would suggest that, at high oxygen fugacities, the substitution $Na_1Fe^{2+}{}_1Fe^{3+}{}_{-1}\square^{A}{}_{-1}$ may play a prominent role. This substitution mechanism was proposed first for dehydration of riebeckite (Ungaretti, 1980) and then again for the dehydrogenation of igneous amphiboles (Phillips et al., 1988), but was found to be less important for Fe^{3+} substitution in natural amphiboles compared to substitutions involving other cations in the M1-3 sites and hydrogen in the O3 site (e.g., Dyar et al., 1993; Popp et al., 1995a; King et al., 1999). In our high f_{O2} experiments, substitution with A-site sodium may be necessary because of a structural limitation on the oxylation of the O3 site caused by preferential incorporation of Fe^{3+} over Ti in the M3 site (e.g., Hawthorne and Oberti, 2007; Oberti et al., 2007). The relatively low

Ti content of amphiboles synthesized at high f_{O2} may be related to the increased stability and abundance of titanomagnetite, which preferentially partitions Ti^{4+} from the melt at these more oxidizing conditions. Low titanium amphiboles were also observed in equilibrium with titanomagnetite by King et al. (2000). Alternatively, the substitution mechanism $0.5H_2+Ti^{4+}+O^{2-} \leftrightarrow Fe^{3+}+OH^-$ has been proposed as one of the dominant mechanisms for Fe^{3+} substitution in the past (e.g., Aoki, 1963; Boettcher and O'Neil, 1980; Dyar et al., 1992).

Fe^{2+} Partitioning between amphibole and melt

Fe^{2+} is compatible in amphibole. It is relatively less compatible than Fe^{3+} for basalts and andesites and relatively more compatible in dacites, as evidenced by the compatibility of Fe^{2+} in amphibole increasing with decreasing NBO/T (**Figure 6**). The compatibility of Fe^{2+} is also somewhat temperature dependent, as evidenced by a weak negative correlation with experimental temperature for andesite and dacite starting compositions. However, the temperature dependence of the Fe^{2+} partition coefficient could also be caused by changes in melt composition that invariably accompany changes in temperature, and we cannot distinguish these effects unequivocally from the data. The temperature dependence of D^{Fe2+} is less pronounced than its dependence on melt viscosity, or NBO/T.

The relationship between melt viscosity or NBO/T and D^{Fe2+} can be modeled as an exponential (**Figure 6**). NBO/T is also exponentially related to D^{Mg} in our experiments (**Figure 6**). Similar exponential relationships between NBO/T and the amphibole-melt partition coefficients of large ion lithophile elements (LILE), rare earth elements (REE), and high field strength elements (HFSE) have been observed (e.g., Klein et al., 1997; Tiepolo et al., 2007). Notably, the Fe^{2+} and Mg mineral-melt partition coefficients of olivine and clinopyroxene have

410 also been found to have exponential relationships with melt NBO/T (e.g., Kushiro and Mysen,
411 2002; Toplis and Corgne, 2002). The similar relationship between D^{Fe2+}, D^{Mg}, and melt viscosity
412 from this study of amphibole and from other studies of common silicate minerals suggests
413 similar changes in the behavior of these elements with melt viscosity, as observed in our
414 experiments.

415 In contrast to the exponential relationship of D^{Fe2+} and D^{Mg} with NBO/T, $K^{Fe2+/Mg}$ (the
416 ratio of D^{Fe2+} and D^{Mg}) is relatively constant (on average, 0.27; **Figure 6**) and identical to the
417 $K^{Fe/Mg}$ for clinopyroxene (Putirka, 2007). The consistency of $K^{Fe2+/Mg}$ in amphibole in our study
418 is similar to the consistent $K^{FeTotal/Mg}$ of olivine in the literature and stands in stark contrast to the
419 relatively scattered $K^{FeTotal/Mg}$ of amphibole in the literature (**Figure 8**). The scatter in amphibole
420 $K^{FeTotal/Mg}$ has also been observed by Putirka (2016) who attributed it to a relatively slow rate of
421 equilibration for amphibole; however, we view the scatter in amphibole $K^{FeTotal/Mg}$ as
422 highlighting the importance of considering Fe^{2+} when calculating distribution coefficients for
423 minerals with Fe^{3+}. Other researchers have emphasized that the Fe-Mg distribution coefficient
424 for olivine is dependent on the Fe^{3+} content of olivine, and variability in the already well-
425 constrained $K^{FeTotal/Mg}$ for olivine is diminished when considering $K^{Fe2+/Mg}$ instead (Blundy et al.,
426 2020). The effect of considering Fe^{2+} in the calculation of the amphibole distribution coefficient
427 is greater because Fe^{3+} is more compatible in amphibole than in olivine and the difference
428 between Fe_{Total} and Fe^{2+} must thus also be greater.
429

430 **Application of $K^{Fe3+/Fe2+}$ as an oxybarometer**

431 The utility of our experimentally determined $K^{Fe3+/Fe2+}$ as an oxybarometer is
432 demonstrated by using it to calculate a range of magmatic f_{O2} at Shiveluch volcano. The mean

433 Fe^{3+}/Fe^{2+} of the melt in equilibrium with each of 11 samples was calculated by multiplying the
434 average Fe^{3+}/Fe^{2+} of amphibole in the sample (calculated from the average Fe^{3+}/Fe_{Total}
435 determined from XAFS analyses and the average wt % FeO found from EPMA analysis) by the
436 average $K^{Fe3+/Fe2+}$ for basalt determined from our experimental study. The Fe^{3+}/Fe^{2+} of the melt
437 was translated to an oxygen fugacity relative to NNO using equation 7 of Kress and Carmichael
438 (1991) and the equation for fugacity at the NNO buffer from O'Neill and Pownceby (1993). The
439 inputs to the equation were sample's average Fe^{3+}/Fe^{2+}_{melt} (determined in the last step), whole
440 rock Al_2O_3, FeO, CaO, Na_2O, and K_2O converted to mole fraction; a temperature of 1062°C; and
441 a pressure of 550 MPa. The temperature and pressure are the average temperature and pressure
442 of amphibole crystallization reported by Goltz et al. (2020).

443 Calculated oxygen fugacity for our sample set has a considerable range, from NNO+1.9
444 to NNO+4 (**Figure 9; Table 6**). This range overlaps with estimates of the oxygen fugacity of
445 andesitic lavas erupted in 2001 (NNO+1.5-2.1; Humphreys et al., 2006). The central assumption
446 of the above calculation is that the Fe^{3+}/Fe_{Total} of amphibole is primitive and reflects the oxygen
447 fugacity of equilibrium melts; it does not account for secondary alteration of Fe^{3+} in amphibole,
448 which will be thoroughly discussed in following sections and which we will show is our
449 preferred interpretation of the upper range of calculated oxygen fugacity. Two samples,
450 amphibole-bearing cumulate 16B and the 3600 BP tephra, have the lowest calculated f_{O2} of our
451 sample set and, on average, overlap with the estimates for oxygen fugacity from Humphreys et
452 al. (2006). We interpret these samples as being reflective of the primitive f_{O2} of magmas at
453 Shiveluch, ~NNO+2. Samples with higher f_{O2} (i.e., all analyzed mafic enclaves and amphibole-
454 bearing cumulate 04L) may reflect actual variability in magmatic f_{O2} caused by mantle source

heterogeneity, differential slab fluid contribution, or crustal processes; the samples could also reflect secondary alteration/dehydrogenation of amphibole in the enclaves.

Calculated f_{O2} is not reflective of real variability and changes in magmatic f_{O2}

We first consider the notion that the range in calculated f_{O2} in our sample set is reflective of real variability in magmatic f_{O2} at Shiveluch. The potential contributions of mantle source heterogeneity, slab fluids, and crustal processes (i.e., fractional crystallization and crustal assimilation) are evaluated for these samples in the context previously published geochemical and petrological measurements and observations of these samples (Goltz et al., 2020 for enclaves and cumulates and Ponomareva et al., 2007 and Volynets et al., 1997 for the tephra).

We use the V/Sc ratio of our samples to determine if mantle source heterogeneity in f_{O2} may be responsible for the heterogeneity in our samples' calculated f_{O2}. The vanadium to scandium ratio of primitive melts is strongly dependent on the oxygen fugacity of their mantle source because of the changes in the partitioning behavior of vanadium with oxygen fugacity due to changes in its valence state (e.g., Lee et al., 2005; Mallmann and O'Neill, 2009). Assuming that the enclaves and tephra were generated through similar degrees of melting of mantle peridotite and that fractional crystallization did not significantly alter the samples' V/Sc, differences in V/Sc would be largely attributable to differences in source f_{O2}. The enclaves and tephra have a smaller range in V/Sc (6.7-7.6) than would be expected from the wide range of f_{O2} calculated from the amphibole Fe^{3+}/Fe^{2+} (a range of >5 V/Sc; Lee et al., 2005), meaning that the samples in this study likely had similar primary f_{O2}, and that the observed range is not a function of mantle source f_{O2} heterogeneity.

The Ba/Th ratio of our samples is used as a proxy to understand the influence of slab fluids on magmatic f_{O2} in our samples. Fluids from mineral dehydration reactions in the downgoing slab contain solutes that are thought to be oxidants and have been used to explain the higher average f_{O2} of arc magmas relative to mid-ocean ridge basalts (MORB; e.g., Parkinson and Arculus, 1999; Kelley and Cottrell, 2009; Brounce et al., 2014; Iacovino et al., 2020; Gaborieau et al., 2020), though the claim that fluids and their solutes are the cause of the higher than average magmatic f_{O2} is debated (e.g., Carmichael, 1990; Lee et al., 2005; Gaetani, 2016). Barium—a large-ion lithophile and fluid-mobile element—is considered a proxy for fluid contribution from the downgoing slab. In the most general sense, the higher a melt's concentration of Ba, the higher its expected water content, although this generalization does not hold true when comparing variation in Ba and H_2O content in arc volcanoes worldwide (e.g., Plank et al., 2013) due to variability in the composition of certain downgoing sediments in which Ba is enriched (e.g., Plank and Langmuir, 1998). In order to separate sediment and fluid signals, we use the ratio of barium to thorium, a relatively fluid-immobile element; this ratio has been used with success in the interpretation of fluid and sediment signals at other arcs (e.g., Patino et al., 2000). If variable melt water content caused the variability in calculated f_{O2} in our samples, a positive correlation between Ba/Th and calculated f_{O2} would be expected. **Figure 10** shows that there is no correlation between Ba/Th and calculated f_{O2}. The lack of correlation between Ba/Th and f_{O2} suggests that melt water content cannot account for the observed range in f_{O2}.

Crustal processes—including fractional crystallization, crustal assimilation, and magma mixing—are also thought to affect the f_{O2} of melts at subduction settings. Fractional crystallization throughout the crustal column has been proposed to "auto-oxidize" primitive melts through the preferential fractionation of Fe^{2+} compared to Fe^{3+} (e.g., Ulmer et al., 2018;

Tang et al., 2018). However, such auto-oxidative effects have not been observed in natural samples at arc settings (e.g., Kelley and Cottrell, 2012; Brounce et al., 2014; Grocke et al., 2016). There is no correlation between whole rock differentiation indices (i.e., MgO and SiO_2) and calculated f_{O2} in our sample set (**Figure 10**). The lack of correlation between f_{O2} and differentiation indices suggests that variability in calculated f_{O2} in our sample set cannot be attributable to magmatic differentiation.

The presence of plagioclase xenocrysts in enclaves with higher calculated f_{O2} and the lack thereof in samples with relatively low calculated f_{O2} may suggest that crustal assimilation increased magmatic f_{O2}. Assimilation of oxidized crustal material has been suggested as a mechanism for the oxidation of melts throughout the crustal column (e.g., Ague and Brimhall, 1988; Lee et al., 2005; Lee et al., 2012); however, a recent study of the oxidation state of evolved Central Andean magmas (known for their relatively high degree of crustal assimilation; e.g., Hildreth and Moorbath, 1988) showed that crustal assimilation alone could not account for a >3 log unit range in f_{O2} in those samples (Grocke et al., 2016).

Xenocrystic plagioclase in the enclaves at Shiveluch is evidence of contamination with more evolved material (either partially crystalline andesite or intermediate to felsic crust). On average, the enclaves have a higher calculated f_{O2} than the cumulate sample 16B and the 3600 BP tephra, which lack evidence for extensive crustal assimilation (Volynets et al., 1997; Goltz et al., 2020). A calculation of the amount of magnetite needed in a crustal assimilant to oxidize the enclaves from ~NNO+2 (the average f_{O2} preserved in amphibole in 16B and the 3600 BP tephra, inferred to be the primitive oxygen fugacity of magmas at Shiveluch) to their measured oxygen fugacity shows that crustal assimilation alone cannot account for the relatively high f_{O2} calculated from amphiboles in the enclaves (see **Supplementary Text**). In conclusion, the

523 variable, high f_{O2} calculated from amphibole in mafic enclaves in our sample set is not likely
524 reflective of real variability in magmatic f_{O2}. The f_{O2} of primitive magmas at Shiveluch is
525 interpreted to be equivalent to the lowest f_{O2} samples, ~NNO+2. In the following section, we
526 evaluate the possibility that the relatively high average Fe^{3+}/Fe_{Total} in the enclaves is reflective
527 not of primitive magmatic f_{O2} but of secondary alteration and hydrogen loss during residence in a
528 hot zone in the shallow crust.
529
530 **Tracking multiple episodes of mafic recharge using dehydrogenation of amphibole**
531 Loss of hydrogen from amphibole is primarily accompanied by a corresponding increase
532 in Fe^{3+} by the substitution
533 $$OH^- + Fe^{2+} \leftrightarrow Fe^{3+} + O^{2-} + \tfrac{1}{2} H_2$$
534 (Dyar et al., 1993; Popp et al., 1995b). Amphibole dehydrogenation can occur as a result of re-
535 equilibration with magmas at different pressures, temperatures, f_{O2}, and/or f_{H2} than the liquid
536 with which the primary amphibole was in equilibrium (e.g., Dyar et al., 1993; Miyagi et al.,
537 1998; King et al., 1999), and the rate of amphibole dehydrogenation is limited by the rate of
538 diffusion of hydrogen through amphibole (Graham 1981; Graham et al., 1984). Dehydrogenation
539 of amphibole in the enclaves could occur after the mafic liquids were quenched in the andesite
540 host magma before eruption and would increase the amphibole Fe^{3+}/Fe_{Total}. Pre-eruptive
541 amphibole dehydrogenation during sub-solidus ascent of mafic enclaves could explain the
542 relatively high average amphibole Fe^{3+}/Fe_{Total} in the enclaves.
543 We model the loss of hydrogen from amphibole as a solid-state diffusive process. The
544 assumption for our calculations is that dehydrogenation initiated when the mafic magmas were
545 injected into the host andesite and quenched as enclaves. The relatively shallow depth and lower

546 water content of the andesite relative to the mafic parents are conducive to amphibole
547 dehydrogenation during sub-solidus ascent (e.g., King et al., 2018). The glassy, rapidly quenched
548 texture of the enclaves and the lack of breakdown rims around amphibole crystals implies that
549 they were not slowly cooled below the amphibole-in curve (Humphreys et al., 2006; King et al.,
550 2018; Goltz et al., 2020). In our calculation, we assume that the average amphibole in the
551 enclaves initially had Fe^{3+}/Fe_{Total} equal to the average of amphibole in the most reduced sample,
552 16B (35.1%) and calculate the percent dehydrogenation required to oxidize amphibole from this
553 starting condition to its average measured Fe^{3+}/Fe_{Total} (40.7-59.1%; **Table 6**). We calculate the
554 amount of hydrogen in the undehydrogenated amphibole using the equation of King et al. (1999)
555 and the Ti, Al^{VI}, and Fe^{3+} of the average amphibole in each sample on a 24 oxygen per formula
556 unit basis, given a Fe^{3+}/Fe_{Total} equal to 35%. The moles of hydrogen lost (equal to the difference
557 in moles of Fe^{3+} in the amphibole with Fe^{3+}/Fe_{Total}=35% and with the average measured
558 Fe^{3+}/Fe_{Total} in the sample) relative to the amount to the moles of hydrogen in the
559 undehydrogenated amphibole is used as a target for forward modeling of hydrogen diffusion,
560 thus allowing us to calculate the amount of time necessary between mafic magma injection and
561 eruption to account for the average Fe^{3+}/Fe_{Total} of amphibole in each enclave, as described below.
562 Percent dehydrogenation ranged from 6.5% to 25%, which corresponds to a 6% to 22% change
563 in Fe^{3+}/Fe_{Total}. This difference in Fe^{3+}/Fe_{Total} is not detectible given the accuracy of our
564 technique, and, as a consequence, observable zoning in Fe^{3+}/Fe_{Total} is not expected.
565 The average residence time of each enclave in the andesite host magma at Shiveluch is
566 calculated by solving for time (t) in the approximate solution of the diffusion equation for an
567 infinite cylinder with radius, a, and fractional loss, f, (Crank, 1975); this approximation is valid

This is the peer-reviewed, final accepted version for American Mineralogist, published by the Mineralogical Society of America.
The published version is subject to change. Cite as Authors (Year) Title. American Mineralogist, in press.
DOI: https://doi.org/10.2138/am-2022-8031. http://www.minsocam.org/

for values of *f* between 0-0.6 where 0 corresponds to zero hydrogen loss and 1 would be complete hydrogen loss from amphibole:

$$f \cong \left(\frac{4}{\sqrt{\pi}}\right)\left(\frac{Dt}{a^2}\right)^{0.5} - \left(\frac{Dt}{a^2}\right) \quad (1)$$

where *D* is the diffusion coefficient for H in amphibole. Fractional loss, *f*, was equal to percent dehydrogenation (see last paragraph) in our calculation. Reported time is the lower of the two roots of this quadratic equation. We used the solution for an infinite cylinder because it is a simple geometry that closely resembles the geometry of acicular amphibole crystals, which have one short and one long dimension in 2D space. Following the analogy between infinite cylinder and acicular amphibole geometries, the radius *a* of the infinite cylinder is akin to the short dimension of the amphibole crystal. In our calculation, *a* was set equal to 417 μm; it was calculated by dividing the average long edge of acicular amphiboles with measured Fe^{3+}/Fe_{Total} (1100 μm) by the average aspect ratio of 58 large (i.e., "long edge"≥1.5 mm) amphiboles measured in hand sample (on average, 2.64). The infinite cylinder geometry is an imperfect geometric analogy to amphibole, however, because there is diffusion at all interfaces in an amphibole crystal (i.e., it does not have an infinite dimension), the time calculated using the infinite cylinder model is likely an upper bound.

Another limitation of our calculation is that anisotropic diffusion is not considered, although a study of kaersutite crystals shows that hydrogen diffusion along the long amphibole c-axis is five times faster than along the short b-axis (Ingrin and Blanchard, 2000). We use a diffusion coefficient, *D*, determined by Graham et al. (1984) for bulk diffusion of H through amphibole; the value is an average rate of diffusion for the crystal irrespective of crystallographic orientation and is appropriate for our modified 1D model. Graham et al. (1984) found an Arrhenius relationship between log*D* and reciprocal temperature for various

591 compositions of amphibole modeled as infinite cylinders or half-sheets as linear. We use their
592 equation of a line for hornblende #3224 modeled as an infinite cylinder:

$$\log D = -7.62 - 4.39\left(\frac{10^3}{T}\right)$$

593 where T is temperature in degree Kelvin and D is in cm^2/s. Four our model, the diffusivity was
594 calculated with a temperature of 840°C, which is the average temperature of the andesite host
595 magma at Shiveluch determined by multiple geothermometers (Dirksen et al., 2006; Humphreys
596 et al., 2006).

597 Uncertainty in time was quantified using a Monte Carlo approach, wherein t was
598 calculated for each sample using 10,000 random, normally distributed points centered around the
599 samples' mean amphibole major element composition from probe analyses and mean amphibole
600 Fe^{3+}/Fe_{Total}, with a standard deviation equal to 2 times the standard error of those quantities.
601 Among the 10,000 generated compositions, points with percent dehydrogenation less than 0 were
602 excluded from the calculation of time. This filter impacted only two samples with relatively low
603 average Fe^{3+}/Fe_{Total}, 09a and 02b; for these two samples, 124 and 18 points were excluded (i.e.,
604 the lowest 1.24% and 0.18% of values), respectively. The filtering of this relatively low
605 percentage of points has a negligible impact on the final calculated time. Because equation 2 is
606 non-linear in time, the distribution of calculated times is not symmetric, so we report the median
607 and interquartile range (IQR) of times rather than the mean and standard deviation (**Table 6,**
608 **Figure 11a,b**).

609 Enclave residence time in the andesite host ranges from 6 days (sample 09a) to 3.4
610 months (sample 04k; **Table 6, Figure 11a**). The range of residence times shows a history of pre-
611 eruptive mafic recharge on the timescale of days to months, consistent with findings based on
612 high Mg olivine xenocrysts and plagioclase phenocrysts in the host andesite erupted in 2001

613 from Shiveluch (Dirksen et al., 2006; Humphreys et al., 2006). There are at minimum three
614 resolvable pulses of mafic recharge in our data: one at 6-13 days before eruption, one at a month
615 before eruption, and another 2-3 months before eruption. We determined the residence times for
616 8 samples and then compared each sample with each other, a total of 28 unique pairs
617 (**Supplementary Figure 1**). The residence times for a pair of samples is distinguishable if the
618 95% confidence envelope of the difference in their median residence times did not overlap zero
619 (**Figure 11c**). To do so, we found the difference between the 10,000 residence times calculated
620 for each of 28 pairs of samples and calculated the median difference and the 95% confidence
621 interval with the minimum width in the distribution. Our results (**Figure 11c**) show two groups
622 of samples with indistinguishable residence times within 95% confidence: samples 04d, 04b,
623 04k, and 5 (red colors in Figure 11) and samples 09a, 02b, and 06a (blue colors in Figure 11).
624 Sample 09a overlaps with sample 02b, but not sample 06a, meaning that, while the three samples
625 had similar residence times in the host andesite, sample 09a may have been injected at a slightly
626 earlier time. Sample 15f (yellow in Figure 11a) overlaps with samples in neither group and was
627 injected into the andesite at a time intermediate between the two groups. Overall, samples with
628 similar residence times were likely injected into a hot, shallow andesite storage region at around
629 the same time.

630 Mafic enclave samples with similar residence time but variable bulk rock differentiation
631 indices (i.e., Mg#) indicate the existence of multiple mafic recharge bodies in the plumbing
632 system under Shiveluch at various states of fractional crystallization evolution. There is no
633 correlation between differentiation index and percent dehydrogenation (**Figure 11a**) within these
634 two groups of enclaves. This indicates that the recharge magmas injected to the andesite at a
635 given time do not represent liquids evolving along a liquid line of descent of a single mafic

636 recharge magma. To account for the distribution in magma composition at a given time of
637 recharge, two to three distinct magma storage areas with variable Mg# must have recharged the
638 andesitic magma over a small time interval.

639 We interpret the enclaves to represent contributions from different mafic magma storage
640 regions in the crust over time, and identify a minimum of three distinct times when the andesite
641 was recharged with at least two mafic recharge magmas of differing composition, within two
642 weeks of, a month before, and two to three months before eruption (**Figure 12**). The mafic
643 magma bodies may be related to a single parental magma in the deep crust that feeds multiple
644 sills at shallower levels; this possibility requires evaluation in future studies.

645

646 **Implications**

647 In this study, we develop the Fe^{3+}/Fe^{2+} partitioning behavior between synthetic amphiboles and
648 melt as an oxybarometer applicable to hydrous magmas at subduction settings, and apply it to
649 amphibole in mafic enclaves, cumulates, and tephra erupted from Shiveluch volcano in
650 Kamchatka. This study proffers a single mineral-melt oxybarometer applicable to rocks with
651 compositions ranging from basalt to dacite. We suggest that researchers seeking to apply our
652 oxybarometer take care to analyze amphibole in rocks that are known to have been rapidly
653 quenched upon eruption, which more reliably preserve magmatic f_{O2} than amphibole in more
654 slowly cooled rocks (King et al., 1999; King et al., 2018). For those who are looking to apply
655 this oxybarometer to compositions intermediate, higher, or lower in NBO/T to the compositions
656 in this study, we recommend applying the NBO/T-independent amphibole-melt Fe^{2+}/Mg
657 partition coefficient as an oxybarometer using an estimate of melt Mg content.

658 For rocks where the magmatic oxygen fugacity is known independently, the partition
659 coefficients determined in our study will also allow researchers to quantitatively determine the
660 Fe^{3+}/Fe^{2+} of amphibole in their samples without direct measurement. This is a great improvement
661 over the limited accuracy of Fe^{3+} determinations by site occupancy calculation from electron
662 microprobe data. We also show the importance of explicitly considering Fe^{2+} in calculation of an
663 Fe-Mg distribution coefficient for amphibole; using Fe^{2+} as opposed to total iron in this situation
664 leads to a much more consistent Fe-Mg distribution coefficient ($K^{Fe\text{-}Mg}$) for amphibole, which
665 has proven to be a very useful petrological quantity for other Fe-Mg silicates. Finally, our
666 analysis and diffusion modeling of amphibole in mafic enclaves has implications for temporal
667 links between mafic recharge and eruption. Our results capture a prolonged period of pre-
668 eruptive mafic recharge and show that each discernable mafic recharge event is not necessarily
669 linked to an eruption at this volcano. Our finding extends the timeframe for pre-eruptive mafic
670 recharge events inferred by other studies based on petrography, crystal chemistry, and modeling
671 (e.g., Murphy et al., 2000; Browne et al., 2006; Ruprecht et al., 2008; Koleszar et al., 2012). The
672 Fe^{3+} content of amphibole is thus a flexible tool that can be used to understand magmatic
673 conditions and plumbing systems in greater detail.
674

675 **Acknowledgements**

676 This research used Beamline 13-IDE of the Advanced Photon Source, a U.S. Department of
677 Energy (DOE) Office of Science User Facility, operated for the DOE Office of Science by
678 Argonne National Laboratory under Contract No. DE-AC02-06CH11357. This research also
679 used the XFM Beamline of the National Synchrotron Light Source II, a U.S. Department of
680 Energy (DOE) Office of Science User Facility operated for the DOE Office of Science by

Brookhaven National Laboratory under Contract No. DE-SC0012704. The authors acknowledge support from Washington University in St. Louis for funding field and lab work associated with this project. AEG acknowledges the McDonnell Center for the Space Sciences for funding. MJK acknowledges support from National Science Foundation EAR Grant #1654683. MCM and MDD acknowledge funding from NASA grants NNX17AL07G and 80NSSC19K19K1008 and National Science Foundation EAR partner grants #1754261 (MDD) and #1754268 (MCM). MDD, MJK, and MCM also acknowledge support from National Science Foundation EAR partner grants #20452 (MDD), #204386 (MJK), and #2042421 (MCM). The authors thank Tony Lanzirotti, Matt Newville, Ryan Tappero, and Sarah Nicholas for their help with collection of XAFS data, and Cai Ytsma for her help with XAFS data processing. Paul Carpenter is thanked for help with and good humor during the collection of microprobe analyses. We also thank Helene Craigg and Kelsey Prissel for their help and support in the lab and during data collection at NSLS-II and APS. Noah McLean is also thanked for discussions on and help with statistical analysis of our dataset. Penny King and an anonymous reviewer are thanked for their constructive and considerate comments on an earlier draft of our manuscript, which indubitably improved its quality.

References

Adam, J., Oberti, R., Cámara, F. and Green, T.H. (2007) An electron microprobe, LAM-ICP-MS and single-crystal X-ray structure refinement study of the effects of pressure, melt-H2O concentration and f O2 on experimentally produced basaltic amphiboles. European Journal of Mineralogy, 19, 641-655

703 Ague, J.J. and Brimhall, G.H. (1988) Magmatic arc asymmetry and distribution of anomalous
704 plutonic belts in the batholiths of California: Effects of assimilation, crustal thickness, and depth
705 of crystallization. Geological Society of America Bulletin, 100, 912-927
706 Aoki, K. (1963) The kaersutites and oxykaersutites from alkalic rocks of Japan and surrounding
707 areas. Journal of Petrology, 4, 198-210
708 Arculus, R.J. and Wills, K.J. (1980) The petrology of plutonic blocks and inclusions from the
709 Lesser Antilles island arc. Journal of Petrology, 21, 743-799
710 Armstrong, J.T., Donovan, J. and Carpenter, P. (2013) CALCZAF, TRYZAF and CITZAF: The
711 use of multi-correction-algorithm programs for estimating uncertainties and improving
712 quantitative X-ray analysis of difficult specimens. Microscopy and Microanalysis, 19, 812-813
713 Ballhaus, C., Berry, R. and Green, D. (1990) Oxygen fugacity controls in the Earth's upper
714 mantle. Nature, 348, 437-440
715 Barclay, J., Rutherford, M.J., Carroll, M., Murphy, M., Devine, J., Gardner, J. and Sparks, R.
716 (1998) Experimental phase equilibria constraints on pre-eruptive storage conditions of the
717 Soufriere Hills magma. Geophysical Research Letters, 25, 3437-3440
718 Beard, J.S. (1986) Characteristic mineralogy of arc-related cumulate gabbros: implications for
719 the tectonic setting of gabbroic plutons and for andesite genesis. Geology, 14, 848-851
720 Bédard, J.H. (2010) Parameterization of the Fe/Mg exchange coefficient (Kd) between
721 clinopyroxene and silicate melts. Chemical Geology, 274, 169-176
722 Blundy, J., Melekhova, E., Ziberna, L., Humphreys, M.C.S., Cerantola, V., Brooker, R.A.,
723 McCammon, C.A., Pichavant, M. and Ulmer, P. (2020) Effect of redox on Fe-Mg-Mn exchange
724 between olivine and melt and an oxybarometer for basalts. Contributions to Mineralogy and
725 Petrology, 175, 1-32

726 Boettcher, A. and O'neil, J. (1980) Stable isotope, chemical, and petrographic studies of high-
727 pressure amphiboles and micas: evidence for metasomatism in the mantle source regions of
728 alkali basalts and kimberlites. American Journal of Science, 280, 594-621
729 Botcharnikov, R.E., Koepke, J., Holtz, F., McCammon, C. and Wilke, M. (2005) The effect of
730 water activity on the oxidation and structural state of Fe in a ferro-basaltic melt. Geochimica et
731 Cosmochimica Acta, 69, 5071-5085
732 Brounce, M., Kelley, K. and Cottrell, E. (2014) Variations in Fe3+/∑ Fe of Mariana Arc basalts
733 and mantle wedge f O2. Journal of Petrology, 55, 2513-2536
734 Browne, B., L., Eichelberger, J.C., Patino, L.C., Vogel, T.A., Dehn, J., Uto, K. and Hoshizumi,
735 H. (2006) Generation of Porphyritic and Equigranular Mafic Enclaves During Magma Recharge
736 Events at Unzen Volcano, Japan. Journal of Petrology, 47, 301-328
737 Bucholz, C.E., Gaetani, G.A., Behn, M.D. and Shimizu, N. (2013) Post-entrapment modification
738 of volatiles and oxygen fugacity in olivine-hosted melt inclusions. Earth and Planetary Science
739 Letters, 374, 145-155
740 Buddington, A. and Lindsley, D. (1964) Iron-titanium oxide minerals and synthetic equivalents.
741 Journal of Petrology, 5, 310-357
742 Carey, C., Dyar, M., Boucher, T. and Giguere, S. (2017) Web-based software for preprocessing,
743 matching, fitting, prediction, and visualization of spectroscopic data: the data exploration,
744 visualization, and analysis of spectra (DEVAS) website. LPI, 1097
745 Carmichael, I.S. (1991) The redox states of basic and silicic magmas: a reflection of their source
746 regions?. Contributions to Mineralogy and Petrology, 106, 129-141
747 Coltorti, M., Bonadiman, C., Faccini, B., Gregoire, M., O'Reilly, S.Y. and Powell, W. (2007)
748 Amphiboles from suprasubduction and intraplate lithospheric mantle. Lithos, 99, 68-84

749 Core, D.P., Kesler, S.E. and Essene, E.J. (2006) Unusually Cu-rich magmas associated with
750 giant porphyry copper deposits: Evidence from Bingham, Utah. Geology, 34, 41-44
751 Cottrell, E. and Kelley, K.A. (2013) Redox heterogeneity in mid-ocean ridge basalts as a
752 function of mantle source. Science, 340, 1314-1317
753 Cottrell, E., Lanzirotti, A., Mysen, B., Birner, S., Kelley, K.A., Botcharnikov, R., Davis, F.A.
754 and Newville, M. (2018) A Mössbauer-based XANES calibration for hydrous basalt glasses
755 reveals radiation-induced oxidation of Fe. American Mineralogist: Journal of Earth and Planetary
756 Materials, 103, 489-501
757 Crank, J. (1975) The mathematics of diffusion, 421 p. Oxford University Press, London
758 Dalpé, C. and Baker, D.R. (2000) Experimental investigation of large-ion-lithophile-element-,
759 high-field-strength-element-and rare-earth-element-partitioning between calcic amphibole and
760 basaltic melt: the effects of pressure and oxygen fugacity. Contributions to Mineralogy and
761 Petrology, 140, 233-250
762 Delaney, J., Bajt, S., Dyar, M., Sutton, S., McKay, G. and Roeder, P. (1996) Comparison of
763 Quantitative Synchrotron MicroXANES (SmX) $Fe^{3+}/(Fe^{2+}+ Fe^{3+})$ Results for Amphibole and
764 Silicate Glass with Independent Measurements. In Lunar and Planetary Science Conference
765 Dirksen, O., Humphreys, M.C.S., Pletchov, P., Melnik, O., Demyanchuk, Y., Sparks, R.S.J. and
766 Mahony, S. (2006) The 2001-2004 dome-forming eruption of Shiveluch volcano, Kamchatka:
767 Observation, petrological investigation and numerical modelling. Journal of Volcanology and
768 Geothermal Research, 155, 201-226
769 Donovan, John J and Tingle, Tracy N and others (1996) An improved mean atomic number
770 background correction for quantitative microanalysis. Microscopy and Microanalysis, 2, 1-7

771 Donovan, J., Kremser, D., Fournelle, J. and Goemann, K. (2012) Probe for EPMA: acquisition,
772 automation and analysis. Probe Software, Inc., Eugene, Oregon
773 Dyar, M.D., Breves, E.A., Gunter, M.E., Lanzirotti, A., Tucker, J.M., Carey, C., Peel, S.E.,
774 Brown, E.B., Oberti, R. and Lerotic, M.A.O. (2016) Use of multivariate analysis for synchrotron
775 micro-XANES analysis of iron valence state in amphiboles. American Mineralogist, 101, 1171-
776 1189
777 Dyar, M.D., McGuire, A.V. and Mackwell, S.J. (1992) Fe^{3+}/H^{+} and D/H in kaersutites—
778 Misleading indicators of mantle source fugacities. Geology, 20, 565-568
779 Dyar, M.D., Mackwell, S.J., McGuire, A.V., Cross, L.R. and Robertson, J.D. (1993) Crystal
780 chemistry of Fe^{3+} and H^{+} in mantle kaersutite: Implications for mantle metasomatism. American
781 Mineralogist, 78, 968-979
782 Dyar, M.D. and Ytsma, C.Y. (2021) Effect of data set size on geochemical quantification
783 accuracy with laser-induced breakdown spectroscopy. Spectrochimica Acta Part B, 177, 106073.
784 Gaborieau, M., Laubier, M., Bolfan-Casanova, N., Mccammon, C., Vantelon, D., Chumakov, A.,
785 Schiavi, F., Neuville, D. and Venugopal, S. (2020) Determination of $Fe^{3+}/\sum$ Fe of olivine-hosted
786 melt inclusions using Mossbauer and XANES spectroscopy. Chemical Geology, 119646
787 Gaetani, G.A. (2016) The behavior of $Fe^{3+}/\sum$ Fe during partial melting of spinel lherzolite.
788 Geochimica et Cosmochimica Acta, 185, 64-77
789 Gaillard, F., Scaillet, B., Pichavant, M. and Bény, J. (2001) The effect of water and fO_2 on the
790 ferric--ferrous ratio of silicic melts. Chemical Geology, 174, 255-273
791 Gavrilenko, M., Krawczynski, M., Ruprecht, P., Li, W. and Catalano, J.G. (2019) The quench
792 control of water estimates in convergent margin magmas. American Mineralogist, 104, 936-948

793 Gavrilenko, M., Herzberg, C., Vidito, C., Carr, M.J., Tenner, T. and Ozerov, A. (2016) A
794 calcium-in-olivine geohygrometer and its application to subduction zone magmatism. Journal of
795 Petrology, 57, 1811-1832
796 Goltz, A.E., Krawczynski, M.J., Gavrilenko, M., Gorbach, N.V. and Ruprecht, P. (2020)
797 Evidence for superhydrous primitive arc magmas from mafic enclaves at Shiveluch volcano,
798 Kamchatka. Contributions to Mineralogy and Petrology, 175, 1-26
799 Graham, C.M. (1981) Experimental hydrogen isotope studies III: Diffusion of hydrogen in
800 hydrous minerals, and stable isotope exchange in metamorphic rocks. Contributions to
801 Mineralogy and Petrology, 76, 216-228
802 Graham, C.M., Harmon, R.S. and Sheppard, S.M. (1984) Experimental hydrogen isotope studies:
803 hydrogen isotope exchange between amphibole and water. American Mineralogist, 69, 128-138
804 Greene, A.R., DeBari, S.M., Kelemen, P.B., Blusztajn, J. and Clift, P.D. (2006) A detailed
805 geochemical study of island arc crust: the Talkeetna arc section, south--central Alaska. Journal of
806 Petrology, 47, 1051-1093
807 Grocke, S.B., Cottrell, E., de Silva, S. and Kelley, K.A. (2016) The role of crustal and eruptive
808 processes versus source variations in controlling the oxidation state of iron in Central Andean
809 magmas. Earth and Planetary Science Letters, 440, 92-104
810 Hamilton, D., Burnham, C.W. and Osborn, E. (1964) The solubility of water and effects of
811 oxygen fugacity and water content on crystallization in mafic magmas. Journal of Petrology, 5,
812 21-39
813 Hawthorne, F.C. and Oberti, R. (2007) Amphiboles: crystal chemistry. Reviews in Mineralogy
814 and Geochemistry, 67, 1-54

815 Hildreth, W. and Moorbath, S. (1988) Crustal contributions to arc magmatism in the Andes of
816 central Chile. Contributions to mineralogy and petrology, 98, 455-489
817 Hou, T., Botcharnikov, R., Moulas, E., Just, T., Berndt, J., Koepke, J., Zhang, Z., Wang, M.,
818 Yang, Z. and Holtz, F. (2021) Kinetics of Fe–Ti Oxide Re-equilibration in Magmatic Systems:
819 Implications for Thermo-oxybarometry. Journal of Petrology, 61
820 Humphreys, M.C., Blundy, J.D. and Sparks, R.S.J. (2006) Magma evolution and open-system
821 processes at Shiveluch Volcano: Insights from phenocryst zoning. Journal of Petrology, 47,
822 2303-2334
823 Iacovino, K., Guild, M.R. and Till, C.B. (2020) Aqueous fluids are effective oxidizing agents of
824 the mantle in subduction zones. Contributions to Mineralogy & Petrology, 175
825 Ingrin, J. and Blanchard, M. (2000) Hydrogen mobility in single crystal kaersutite. EMPG VIII.
826 In Journal of Conference Abstracts, p. 52
827 Jagoutz, O., Müntener, O., Schmidt, M.W. and Burg, J. (2011) The roles of flux-and
828 decompression melting and their respective fractionation lines for continental crust formation:
829 evidence from the Kohistan arc. Earth and Planetary Science Letters, 303, 25-36
830 Jiang, G., Zhao, D. and Zhang, G. (2009) Seismic tomography of the Pacific slab edge under
831 Kamchatka. Tectonophysics, 465, 190-203
832 Kajfosz, J. and Kwiatek, W.M. (1987) Nonpolynomial approximation of background in X-ray
833 spectra. Nuclear Instruments and Methods in Physics Research Section B: Beam Interactions
834 with Materials and Atoms, 22, 78-81
835 Kelley, K.A. and Cottrell, E. (2012) The influence of magmatic differentiation on the oxidation
836 state of Fe in a basaltic arc magma. Earth and Planetary Science Letters, 329, 109-121

837 Kelley, K.A. and Cottrell, E. (2009) Water and the oxidation state of subduction zone magmas.
838 Science, 325, 605-607
839 King, P.L., Wheeler, V.M., Renggli, C.J., Palm, A.B., Wilson, S.A., Harrison, A.L., Morgan, B.,
840 Nekvasil, H., Troitzsch, U. and Mernagh, T. (2018) Gas–solid reactions: Theory, experiments
841 and case studies relevant to earth and planetary processes. Reviews in Mineralogy and
842 Geochemistry, 84, 1-56
843 King, P., Hervig, R., Holloway, J., Delaney, J. and Dyar, M. (2000) Partitioning of
844 Fe^{3+}/Fe_{Total} between amphibole and basanitic melt as a function of oxygen fugacity. Earth and
845 Planetary Science Letters, 178, 97-112
846 King, P., Hervig, R., Holloway, J., Vennemann, T. and Righter, K. (1999) Oxy-substitution and
847 dehydrogenation in mantle-derived amphibole megacrysts. Geochimica et Cosmochimica Acta,
848 63, 3635-3651
849 Klein, M., Stosch, H. and Seck, H. (1997) Partitioning of high field-strength and rare-earth
850 elements between amphibole and quartz-dioritic to tonalitic melts: an experimental study.
851 Chemical Geology, 138, 257-271
852 Koleszar, A.M., Kent, A.J., Wallace, P.J. and Scott, W.E. (2012) Controls on long-term low
853 explosivity at andesitic arc volcanoes: Insights from Mount Hood, Oregon. Journal of
854 Volcanology and Geothermal Research, 219, 1-14
855 Krawczynski, M. and Olive, J. (2011) A new fitting algorithm for petrological mass-balance
856 problems. AGUFM, 2011, 53B-2613
857 Kress, V.C. and Carmichael, I.S. (1991) The compressibility of silicate liquids containing
858 Fe_2O_3 and the effect of composition, temperature, oxygen fugacity and pressure on their redox
859 states. Contributions to Mineralogy and Petrology, 108, 82-92

860 Kushiro, I. and Mysen, B.O. (2002) A possible effect of melt structure on the Mg-
861 Fe^{2+} partitioning between olivine and melt. Geochimica et Cosmochimica Acta, 66, 2267-2272
862 Leake, B.E., Woolley, A.R., Birch, W.D., Burke, E.A., Ferraris, G., Grice, J.D., Hawthorne,
863 F.C., Kisch, H.J., Krivovichev, V.G., Schumacher, J.C. and and others (2003) Nomenclature of
864 amphiboles: additions and revisions to the International Mineralogical Association's 1997
865 recommendations. The Canadian Mineralogist, 41, 1355-1362
866 Leake, B.E., Woolley, A.R., Arps, C.E., Birch, W.D., Gilbert, M.C., Grice, J.D., Hawthorne,
867 F.C., Kato, A., Kisch, H.J., Krivovichev, V.G. and and others (1997) Nomenclature of
868 amphiboles; report of the Subcommittee on Amphiboles of the International Mineralogical
869 Association Commission on new minerals and mineral names. Mineralogical magazine, 61, 295-
870 310
871 Lee, C.T.A., Leeman, W.P., Canil, D. and Li, Z.A. (2005) Similar V/Sc systematics in MORB
872 and arc basalts: implications for the oxygen fugacities of their mantle source regions. Journal of
873 Petrology, 46, 2313-2336
874 Lee, C.T.A., Luffi, P., Chin, E.J., Bouchet, R., Dasgupta, R., Morton, D.M., Le Roux, V., Yin,
875 Q. and Jin, D. (2012) Copper systematics in arc magmas and implications for crust-mantle
876 differentiation. Science, 336, 64-68
877 Levin, V., Shapiro, N., Park, J. and Ritzwoller, M. (2002) Seismic evidence for catastrophic slab
878 loss beneath Kamchatka. Nature, 418, 763-767
879 Mallmann, G. and O'Neill, H.S.C. (2009) The crystal/melt partitioning of V during mantle
880 melting as a function of oxygen fugacity compared with some other elements (Al, P, Ca, Sc, Ti,
881 Cr, Fe, Ga, Y, Zr and Nb). Journal of Petrology, 50, 1765-1794

882 Martin, R.F. (2007) Amphiboles in the igneous environment. Reviews in Mineralogy and
883 Geochemistry, 67, 323-358
884 Mathez, E. (1984) Influence of degassing on oxidation states of basaltic magmas. Nature, 310,
885 371-375
886 McCanta, M.C., Rutherford, M.C. and Hammer, J.E. (2007) Pre-eruptive and syn-eruptive
887 conditions in the Black Butte, California dacite: Insight into crystallization kinetics in a silicic
888 magma system. Journal of Volcanology and Geothermal Research, 160, 263-284
889 McGill, R., Tukey, J.W. and Larsen, W.A. (1978) Variations of box plots. The American
890 Statistician, 32, 12-16
891 Miyagi, I., Matsubaya, O. and Nakashima, S. (1998) Change in D/H ratio, water content and
892 color during dehydration of hornblende. Geochemical Journal, 32, 33-48
893 Moore, G., Righter, K. and Carmichael, I. (1995) The effect of dissolved water on the oxidation
894 state of iron in natural silicate liquids. Contributions to Mineralogy and Petrology, 120, 170-179
895 Mungall, J.E. (2002) Roasting the mantle: Slab melting and the genesis of major Au and Au-rich
896 Cu deposits. Geology, 30, 915-918
897 Murphy, M.D., Sparks, R.S.J., Barclay, J., Carroll, M.R. and Brewer, T.S. (2000) Remobilization
898 of Andesite Magma by Intrustion of Mafic Magma at the Soufriere Hills Volcano, Montserrat,
899 West Indies. Journal of Petrology, 41, 21-42
900 Mysen, B.O. (1988) Structure and properties of silicate melts
901 Nikulin, A., Levin, V., Shuler, A. and West, M. (2010) Anomalous seismic structure beneath the
902 Klyuchevskoy Group, Kamchatka. Geophysical Research Letters, 37

Nikulin, A., Levin, V., Carr, M., Herzberg, C. and West, M. (2012) Evidence for two upper mantle sources driving volcanism in Central Kamchatka. Earth and Planetary Science Letters, 321, 14-19

Nishizawa, T., Nakamura, H., Churikova, T., Gordeychik, B., Ishizuka, O., Haraguchi, S., Miyazaki, T., Vaglarov, B.S., Chang, Q., Hamada, M. and and others (2017) Genesis of ultra-high-Ni olivine in high-Mg andesite lava triggered by seamount subduction. Scientific reports, 7, 1-11

Oberti, R., Hawthorne, F.C., Cannillo, E. and Cámara, F. (2007) Long-range order in amphiboles. Reviews in Mineralogy and Geochemistry, 67, 125-171

O'Neill, H.S.C. and Nell, J. (1997) Gibbs free energies of formation of RuO_2, IrO_2, and OsO_2: A high-temperature electrochemical and calorimetric study. Geochimica et Cosmochimica Acta, 61, 5279-5293

O'Neill, H.S.C. and Pownceby, M.I. (1993) Thermodynamic data from redox reactions at high temperatures. I. An experimental and theoretical assessment of the electrochemical method using stabilized zirconia electrolytes, with revised values for the Fe-"FeO", Co-CoO, Ni-NiO and Cu-Cu_2O oxygen buffers, and new data for the W-WO_2 buffer. Contributions to Mineralogy and Petrology, 114, 296-314

Osborn, E.F. (1959) Role of oxygen pressure in the crystallization and differentiation of basaltic magma. American Journal of Science, 257, 609-647

Papale, P., Moretti, R. and Barbato, D. (2006) The compositional dependence of the saturation surface of H_2O+ CO_2 fluids in silicate melts. Chemical Geology, 229, 78-95

924 Park, J., Levin, V., Brandon, M., Lees, J., Peyton, V., Gordeev, E. and Ozerov, A. (2002) A
925 dangling slab, amplified arc volcanism, mantle flow and seismic anisotropy in the Kamchatka
926 Plate Corner. In S. Stein and J.T. Freymueller, Eds., Plate Boundary Zones, p. 295-324. AGU
927 Parkinson, I.J. and Arculus, R.J. (1999) The redox state of subduction zones: insights from arc-
928 peridotites. Chemical Geology, 160, 409-423
929 Parlak, O., Höck, V. and Delaloye, M. (2000) Suprasubduction zone origin of the Pozanti-
930 Karsanti ophiolite (southern Turkey) deduced from whole-rock and mineral chemistry of the
931 gabbroic cumulates. Geological Society, London, Special Publications, 173, 219-234
932 Patino, L.C., Carr, M.J. and Feigenson, M.D. (2000) Local and regional variations in Central
933 American arc lavas controlled by variations in subducted sediment input. Contributions to
934 Mineralogy and Petrology, 138, 265-283
935 Peyton, V., Levin, V., Park, J., Brandon, M., Lees, J., Gordeev, E. and Ozerov, A. (2001) Mantle
936 flow at a slab edge: Seismic anisotropy in the Kamchatka region. Geophysical Research Letters,
937 28, 379-382
938 Phillips, M.W., Popp, R.K. and Clowe, C.A. (1988) Structural adjustments accompanying
939 oxidation-dehydrogenation in amphiboles. American Mineralogist, 73, 500-506
940 Plank, T. and Langmuir, C.H. (1998) The chemical composition of subducting sediment and its
941 consequences for the crust and mantle. Chemical Geology, 145, 325-394
942 Plank, T., Kelley, K.A., Zimmer, M.M., Hauri, E.H. and Wallace, P.J. (2013) Why do mafic arc
943 magmas contain~ 4 wt% water on average?. Earth and Planetary Science Letters, 364, 168-179
944 Ponomareva, V., Kyle, P., Pevzner, M., Sulerzhitsky, L. and Hartman, M. (2007) Holocene
945 Eruptive History of Shiveluch Volcano, Kamchatka Peninsula, Russia. In J.C. Eichelberger, E.

946 Gordeev, P.E. Izbekov, M. Kasahara and J. Lees, Eds., Volcanism and Subduction: The
947 Kamchatka Region, p. 263-282. American Geophysical Union
948 Popp, R.K., Virgo, D., Yoder, H.S., Hoering, T.C. and Phillips, M.W. (1995a) An experimental
949 study of phase equilibria and Fe oxy-component in kaersutitic amphibole: Implications for the
950 fH_2 and aH_2O in the upper mantle. American Mineralogist, 80, 534-548
951 Popp, R.K., Virgo, D. and Phillips, M.W. (1995b) H deficiency in kaersutitic amphiboles:
952 Experimental verification. American Mineralogist, 80, 1347-1350
953 Putirka, K. (2016) Amphibole thermometers and barometers for igneous systems and some
954 implications for eruption mechanisms of felsic magmas at arc volcanoes. American Mineralogist,
955 101, 841-858
956 Putirka, K.D. (2008) Thermometers and Barometers for Volcanic Systems. Reviews in
957 Mineralogy and Geochemistry, 69, 61-120

958 Richards, J.P. (2011) High Sr/Y Arc Magmas and Porphyry Cu±Mo±Au Deposits: Just Add
959 Water. Economic Geology, 106, 1075-1081

960 Rowe, M.C., Kent, A.J. and Nielsen, R.L. (2009) Subduction influence on oxygen fugacity and
961 trace and volatile elements in basalts across the Cascade Volcanic Arc. Journal of Petrology, 50,
962 61-91
963 Ruprecht, P., Bergantz, G.W. and Dufek, J. (2008) Modeling of gas-driven magmatic overturn:
964 Tracking of phenocryst dispersal and gathering during magma mixing. Geochemistry,
965 Geophysics, Geosystems, 9

966 Sisson, T. and Grove, T. (1993) Experimental investigations of the role of H_2O in calc-alkaline
967 differentiation and subduction zone magmatism. Contributions to mineralogy and petrology, 113,
968 143-166
969 Sugawara, T. (2001) Ferric iron partitioning between plagioclase and silicate liquid:
970 thermodynamics and petrological applications. Contributions to Mineralogy and Petrology, 141,
971 659-686
972 Sun, W., Liang, H., Ling, M., Zhan, M., Ding, X., Zhang, H., Yang, X., Li, Y., Ireland, T.R.,
973 Wei, Q. and and others (2013) The link between reduced porphyry copper deposits and oxidized
974 magmas. Geochimica et Cosmochimica Acta, 103, 263-275
975 Tang, M., Erdman, M., Eldridge, G. and Lee, C.A. (2018) The redox "filter" beneat magmatic
976 orogens and the formation of continental crust. Science Advances, 4
977 Tiepolo, M., Oberti, R., Zanetti, A., Vannucci, R. and Foley, S.F. (2007) Trace-element
978 partitioning between amphibole and silicate melt. Reviews in Mineralogy and Geochemistry, 67,
979 417-452
980 Toplis, M.J. and Corgne, A. (2002) An experimental study of element partitioning between
981 magnetite, clinopyroxene and iron-bearing silicate liquids with particular emphasis on vanadium.
982 Contributions to Mineralogy and Petrology, 144, 22-37
983 Ulmer, P., Kaegi, R. and Müntener, O. (2018) Experimentally derived intermediate to silica-rich
984 arc magmas by fractional and equilibrium crystallization at 1.0 GPa: an evaluation of phase
985 relationships, compositions, liquid lines of descent and oxygen fugacity. Journal of Petrology,
986 59, 11-58

987 Ungaretti, L. (1980) Recent developments in X-ray single crystal diffractometry applied to the
988 crystal-chemical study of amphiboles. Godisnjak Jugoslavenskog centra za kristalografiju, 15,
989 29-65
990 Volynets, O., Ponomareva, V. and Babansky, A. (1997) Magnesian basalts of Shiveluch andesite
991 volcano, Kamchatka. Petrology, 5, 206-221
992 Wilke, M., Behrens, H., Burkhard, D.J. and Rossano, S. (2002) The oxidation state of iron in
993 silicic melt at 500 MPa water pressure. Chemical Geology, 189, 55-67
994 Yogodzinski, G., Lees, J., Churikova, T., Dorendorf, F., Wöerner, G. and Volynets, O. (2001)
995 Geochemical evidence for the melting of subducting oceanic lithosphere at plate edges. Nature,
996 409, 500-504
997 Zhang, H., Hirschmann, M., Cottrell, E., Newville, M. and Lanzirotti, A. (2016) Structural
998 environment of iron and accurate determination of $Fe^{3+}/\Sigma Fe$ ratios in andesitic glasses by
999 XANES and Mossbauer spectroscopy. Chemical Geology, 428, 48-58
1000 Zhang, H.L., Cottrell, E., Solheid, P.A., Kelley, K.A. and Hirschmann, M.M. (2018)
1001 Determination of $Fe^{3+}/\Sigma Fe$ of XANES basaltic glass standards by Mossbauer spectroscopy and
1002 its application to the oxidation state of iron in MORB. Chemical Geology, 479, 166-175

Figure 1. (a) Assembly for ½" piston cylinder experiments. ¾" piston cylinder assembly is not shown, but differs in the larger inner diameter of the graphite furnace (and, correspondingly, the outer diameter of MgO parts), taller height, substitution of $BaCO_3$ for NaCl as a pressure medium, and addition of pyrex glass sleeve separating pressure medium and graphite furnace. **(b)** and **(c)** show capsule designs for experiments buffered at NNO or Ru-RuO_2, respectively.

Figure 2. BSE images of experimental products **(a)** F163 **(b)** F179, **(c)** OD109, and **(d**) OD129. Crystalline phases are labeled in (a). Relatively high Z phases in (b) (i.e. bright phases) are titanomagnetite and, at the edge of the grain, Ru and RuO_2 (the buffering assemblage). Crystalline phase in (c) and (d) is amphibole.

Figure 3. Amphibole major element variation diagrams. Color indicates starting composition (blue is basalt, pink is andesite, and grey is dacite) and shape indicates experimental f_{O2} (circles are NNO, triangles are NNO+1, and squares are Ru-RuO_2). There is no discernable trend in major element chemistry with decreasing Mg, but experiments run at higher f_{O2} are relatively lower in Ti, and some are lower in Na.

Figure 4. Plot showing experimental temperature vs. D^{Fe3+} and D^{Fe2+}. For each starting composition, results from only 1 experimental pressure and oxygen fugacity is shown (1 GPa and NNO for basalts and andesites, and 300 MPa and NNO+1 for dacite). There is no apparent effect of temperature on the partitioning of Fe^{3+} or Fe^{2+}, but Fe^{2+} partitioning has a weak temperature dependence in experiments with andesitic and dacite starting compositions. Color and shape are as in Figure 3.

Figure 5. Experimental pressure vs D^{Fe3+} and D^{Fe2+}. There is no discernable effect of pressure on the partitioning of Fe^{3+} or Fe^{2+}. Color and shape are as in Figure 3.

Figure 6. Melt NBO/T vs. D^{Fe3+}, D^{Fe2+}, DMg, $K^{Fe2+/Mg}$, and $K^{Fe3+/Fe2+}$. NBO/T was calculated using the procedure in Mysen (1988) on an anhydrous basis. Melt polymerization has a significant effect on Fe^{2+} partitioning and appears to have an exponential relationship with the partition coefficient. Oxygen fugacity has a minor effect on the partitioning behavior of Fe^{3+}. Color and shape are as in Figure 3. The thick bars in the plot of $K^{Fe3+/Fe2+}$ represent the average partition coefficient for each starting composition, excluding experiments done at the Ru-RuO_2 buffer. Because the high f_{O2} experiments are only indirectly relevant to arc settings, we excluded them from plots showing $K^{Fe2+/Mg}$ and $K^{Fe3+/Fe2+}$.

Figure 7. Box-and-whisker plot summarizing the median, interquartile range, minimum, and maximum values of Fe^{3+}/Fe_{Total} of amphiboles analyzed in mafic enclaves, cumulates, and tephra by sample. Statistical outliers are represented as black dots and were determined using the definition of McGill *et al.* (1978). Averages for each sample (excluding outlier points) are shown as purple points. The number of points represented by the box plot for each sample is shown in red. Grey error bar on far right represents accuracy of Fe^{3+}/Fe_{Total}. Analyses of oxidized crystals have been excluded from this summary.

Figure 8. Fe_{Total}-Mg K_D of amphibole (orange) and olivine (green) reported from the LEPR database. Jitter has been introduced to the x-axis for clarity. The spread of amphibole K_D is much

larger than that of olivine, though the mean value is similar. One potential explanation for the wider distribution of amphibole K_D is the inability to account for Fe^{3+} in amphibole, which would have a significant effect on the Fe^{3+}-bearing amphibole but would minimally affect olivine K_D.

Figure 9. Calculated f_{O2} by sample by increasing calculated oxygen fugacity. Error bars represent the propagated standard deviation of the average ferric-ferrous ratio for each sample. Grey error bar represents uncertainty in f_{O2} calculation propogated from DEVAS predicted Fe^{3+}/Fe_{total} (i.e. the minimum uncertainty). Dashed grey line represents average calculated f_{O2}.

Figure 10. Calculated average f_{O2} vs. whole rock Ba/Th, MgO, and SiO_2. Shape corresponds to sample classification (i.e., cumulate, enclave, or tephra). There is no correlation between any of these variables and the calculated f_{O2}.

Figure 11. (a) Box-and-whisker plot showing median, interquartile range, and extremes of calculated residence time of each sample in an andesitic magma versus sample Mg#. Boxes are centered on the Mg# of each sample, and the width the two more magnesian boxes is narrower because they overlap significantly in Mg#. Red samples have longer median residence times than samples colored blue. Sample 15f, which overlaps with neither group, is colored yellow. There is no correlation between sample Mg# and median residence time. **(b)** Histograms and box-and-whisker plots of calculated residence times for samples 05 (red) and 09a (blue) from Monte Carlo calculations showing how the distribution of points from the calculation translate to the box and whisker visual statistical summary. **(c)** Results of Monte Carlo calculation of 95% confidence interval (CI) and median difference between 28 pairs of samples. Uncertainty is calculated as CI/2. Sample pairs with uncertainty bars (i.e., the 95% confidence interval) overlapping zero (dashed line) have indistinguishable residence times in the host andesite within error. Color corresponds to the relative residence time of samples in the pair. Pairs where both samples have relatively short median residence times are colored blue, pairs where both samples have relatively long median residence times are colored red, pairs where one sample has a relatively short and one sample has a relatively long residence time are colored lilac, pairs with a sample with a short residence time and intermediate sample 15f are colored green, and pairs with a sample with a long residence time and intermediate sample 15f are colored yellow. From this analysis we are able to resolve a minimum of three pulses of magma recharge. We find that samples 09a, 06a, and 02b were injected into the host andesite within two weeks of the eruption and that this group of samples is distinguishable from samples 04b, 04d, 04k, and 5, which recharged the host andesite 2-3 months before eruption. Sample 15f was injected into the host andesite at 1 month before eruption, temporally between the two other groups.

Figure 12. Schematic model for enclave formation and plumbing under Shiveluch over time based on amphibole Fe^{3+}/Fe_{Total}. Colors correspond to relative injection time as in Figure 11 (i.e., blue sills and enclaves are injected at later times than red sills and enclaves) except for the andesite, which is colored grey. From our data, we can resolve a minimum of three pulses of mafic recharge. Compositionally, the magmas injected during each recharge event were at different stages of differentiation and originated from different sills. Sills in this diagram are within the range of depths calculated for amphibole crystallization by Goltz et al. (2020); the maximum depth of the andesite is constrained by Dirksen et al. (2006). **(a)** A magnesian magma

injected to the andesite at an earlier time (red) could be related to a later-injected, less magnesian magma (blue) by fractional crystallization of amphibole (brown), olivine (green), and clinopyroxene (light green) over time; fractional crystallization of these phases relates primitive magmas at this volcano to more evolved melts (Goltz et al., 2020). **(b)** Recharge magmas carry phenocrysts (phases as identified in **(a)**) and crustal cumulates to the shallow andesite. **(c,d)** Upon injection to the andesite, amphibole dehydrogenates; the extent of the dehydrogenation is dependent on the rate of diffusion of H through amphibole and the residence time of the crystal in the shallow andesite. **(c)** and **(d)** show plane polarized light images of sample 06a **(c)** and 04d **(d)** and a vectorized rendering of an amphibole in those samples. The arrow represents dehydrogenation of the amphibole during its residence time; the percent dehydrogenation for 06a is calculated to be 9.3% and is 20.8% for 04d.

Supplementary Figure 1. Histogram matrix of calculated residence times for each of 28 pairs of 8 samples. The distribution of residence times are colored by sample; for each box in the matrix, the pink histogram is of the sample indicated in the column heading (in pink) and the purple histogram is of the sample indicated in row heading (in purple). The overlap between the residence times of samples (visually depicted as the overlap of histograms) is quantified by our calculation of the 95% confidence interval of the difference between the residence times of two samples in a pair (see **Figure 11**).

Table 1. Compositions and descriptions of starting mixes in wt% oxide

Mix No.	Description	Na_2O	MgO	Al_2O_3	SiO_2	MnO	FeO	K_2O	P_2O_5	TiO_2	CaO
53	3600 Tephra Parent	2.66	13.19	12.86	52.80	0.20	8.20	1.49	0.00	0.77	7.83
54	7600 Tephra Parent	2.76	16.32	12.72	52.10	0.17	8.02	0.54	0.21	0.62	6.56
59	7600 Tephra	3.27	9.49	16.04	54.00	0.19	7.50	0.66	0.21	0.75	7.89
60	3600 Tephra	2.74	10.83	13.73	52.56	0.20	8.63	1.64	0.36	0.81	8.51
61	Soufriere Hills Andesite	3.66	2.71	17.49	60.64	0.20	7.11	0.69	0.00	0.61	6.92
BB	Black Butte Dacite	4.70	2.14	17.50	65.62	0.04	3.20	1.14	0.00	0.43	5.23

This is the peer-reviewed, final accepted version for American Mineralogist, published by the Mineralogical Society of America.
The published version is subject to change. Cite as Authors (Year) Title. American Mineralogist, in press.
DOI: https://doi.org/10.2138/am-2022-8031. http://www.minsocam.org/

Table 2. Experimental conditions and phase relations. Bolded experiments report TDI-corrected glass compositions (see Analytical Methods)

ID	Starting Mix	T (°C)	P (GPa)	f_{O2}	CH_2O (wt%)	t (hrs)	Phase (%)
OD143	60-hiK tephra	1060	1	NNO	12.33	48	gl(51)+cpx(24)+amph(11)+opx(11)
OD144	59-loK tephra	1060	1	NNO	8.92	48	gl(67)+amph(13)+opx(16)+cpx(4)
OD102	53-hiK parent	1050	1	NNO	20.17	48	gl(58)+cpx(18)+am(7)+ol(17)
F136	53-hiK parent	1010	1	NNO	19.74	47	gl(45)+am(31)+ cpx(13)+ol(11)
F137	54-loK parent	1010	1	NNO	19.78	48	gl(47)+ol(21)+am(32)
F163	60-hiK tephra	1000	1	NNO	19.56	48	gl(46)+am(38)+cpx(10)+ol(2)+opx(2)
F178	**60-hiK tephra**	**1000**	**1**	**RuRuO2**	**19.56**	**48**	**am(54)+gl(41)+tmnt(4)+cpx(tr)**
OD109	59-loK tephra	1000	1	NNO	19.32	52	gl(58)+am(40)+opx(2)
OD138	60-hiK tephra	1000	1	RuRuO2	17.7	45	am(58)+gl(36)+tmnt(5)+phos(tr)
F174	**60-hiK tephra**	**950**	**0.5**	**NNO**	**10.16**	**48**	**am(63)+gl(34)+opx(2)+phos(1)**
F177	61-Soufriere Andesite	950	0.5	NNO	9.78	48	gl(86)+plag(8)+amph(6)+opx(tr)
F179	**60-hiK tephra**	**950**	**1**	**RuRuO2**	**18.73**	**48**	**am(60)+gl(37)+tmnt(4)*results calculated without sodium***
OD129	61-Soufriere Andesite	950	1	NNO	18.47	48	gl(99)+am(1)+tmnt(tr)
F176	61-Soufriere Andesite	900	0.5	NNO	9.44	49	gl(92)+am(8)+plag(tr)+unreacted corundum
MC69	Black Butte Dacite	900	0.3	NNO+1	6.75	48	gl+plag+am+ox
OD131	61-Soufriere Andesite	900	1	NNO	17.37	49	gl(85)+am(15)+tmnt(tr)
OD139	61-Soufriere Andesite	900	1	RuRuO2	17.37	48	gl(73)+plag(15)+tmnt(6)+am(5)
MC48	Black Butte Dacite	875	0.2	NNO+1	5.46	48	gl+plag+am+opx+cpx+ox
MC49	Black Butte Dacite	850	0.2	NNO+1	5.41	456	gl+plag+am+opx+cpx+ox
MC68	Black Butte Dacite	850	0.3	NNO+1	6.53	96	gl+plag+am+opx+cpx+ox
MC51	Black Butte Dacite	825	0.2	NNO+1	5.34	312	gl+plag+am+opx+cpx+ox

This is the peer-reviewed, final accepted version for American Mineralogist, published by the Mineralogical Society of America.
The published version is subject to change. Cite as Authors (Year) Title. American Mineralogist, in press.
DOI: https://doi.org/10.2138/am-2022-8031. http://www.minsocam.org/

Table 3. Average phase analyses in wt% oxide, Mg#, Fe^{3+}/Fe_{Total}, and Fe/Mg partition coefficients (calculated with all Fe as Fe^{2+}) with 1 standard deviation (sd). Fe^{3+}/Fe_{Total} for amphibole is from XAFS measurements and Fe^{3+}/Fe_{Total} for glasses is calculated using equation 7 of Kress and Carmichael (1991). NBO/T was calculated using equations from Mysen (1988). B.D.L. indicates analysis below detection limit, and NA indicates that starting mix did not include the oxide.

ID	Phase	n	Na_2O	MgO	Al_2O_3	SiO_2	MnO	FeO	K_2O	P_2O_5	TiO_2	CaO	Total	Mg#	Fe^{3+}/Fe_{Total}	K_D Fe/Mg ol	K_D Fe/Mg cpx	Anhydrous NBO/T
OD143	gl	9	1.16	3.44	17.89	50.51	0.14	5.95	1.30	0.56	0.81	6.74	88.45	0.51	16.27		0.24	0.25
	sd		0.13	0.44	0.13	0.23	0.01	0.24	0.34	0.03	0.02	0.32	0.54					
	am	10	2.31	16.14	13.93	42.79	0.14	8.45	1.03	0.04	1.96	11.07	97.86	0.77	31.90			
	sd		0.06	0.40	0.49	0.43	0.01	0.20	0.06	0.01	0.08	0.34	0.16		2.86			
	cpx	7	0.54	16.37	3.14	52.73	0.26	6.81	0.03	0.11	0.50	20.26	100.76	0.81				
	sd		0.16	0.44	0.70	0.32	0.09	0.71	0.02	0.19	0.10	0.52	0.31					
	opx	9	0.03	27.57	3.64	53.64	0.34	13.48	b.d.l.	0.01	0.22	1.65	100.58	0.78				
	sd		0.01	0.43	0.40	0.42	0.02	0.22	b.d.l.	0.01	0.03	0.29	0.29					
OD144	gl	14	0.89	3.06	17.91	50.73	0.15	5.01	0.70	0.28	0.67	7.38	86.73	0.52	15.88		0.24	0.20
	sd		0.24	0.90	0.26	0.62	0.02	0.44	0.28	0.02	0.03	0.50	1.50					
	am	9	2.57	16.95	13.62	44.01	0.16	8.25	0.32	0.02	1.59	10.76	98.24	0.79	32.00			
	sd		0.08	0.36	0.44	0.40	0.01	0.21	0.02	0.01	0.22	0.22	0.27		4.81			
	opx	9	0.05	28.40	4.79	53.16	0.32	11.97	b.d.l.	0.01	0.22	1.69	100.61	0.81				
	sd		0.01	0.55	0.88	0.79	0.01	0.73	b.d.l.	0.01	0.02	0.22	0.37					
	cpx	7	0.47	16.28	3.51	52.48	0.22	6.41	b.d.l.	0.02	0.49	20.86	100.73	0.82				
	sd		0.12	0.44	0.62	0.53	0.01	0.61	b.d.l.	0.02	0.09	0.28	0.60					
OD102	gl	20	2.14	3.43	17.92	50.18	0.14	5.27	1.79	NA	0.91	6.68	88.46	0.54	15.99	0.31	0.22	0.24
	sd		0.15	0.16	0.14	0.33	0.02	0.14	0.18	NA	0.06	0.09	0.40					
	am	6	2.36	16.79	12.93	43.35	0.15	7.90	0.83	NA	1.93	11.42	97.67	0.79	30.42			
	sd		0.09	0.71	0.73	0.84	0.01	0.13	0.05	NA	0.14	0.14	1.17		4.44			
	ol(rims)	11	b.d.l.	40.93	b.d.l.	38.74	0.38	19.35	b.d.l.	NA	0.03	0.13	99.56	0.79				
	sd		b.d.l.	0.77	b.d.l.	0.50	0.02	0.41	b.d.l.	NA	0.01	0.02	0.79					
	cpx	13	0.27	16.67	2.32	52.89	0.20	5.61	0.02	NA	0.41	22.03	100.41	0.84				
	sd		0.08	0.39	0.24	0.86	0.02	0.25	0.01	NA	0.04	0.41	1.06					
	ol(cores, tr)	12	b.d.l.	44.58	0.04	39.85	0.36	15.11	b.d.l.	NA	0.06	0.20	100.20	0.84				
	sd		b.d.l.	1.60	0.04	0.52	0.02	1.69	b.d.l.	NA	0.03	0.10	0.86					
F136	gl	17	1.69	2.72	16.93	53.93	0.15	5.33	1.89	NA	0.59	5.64	88.90	0.48	16.48	0.26	0.22	0.18
	sd		0.27	0.19	0.31	0.95	0.01	0.13	0.13	NA	0.02	0.17	1.24					
	am	22	2.14	16.44	11.63	44.62	0.15	8.30	0.93	NA	1.52	11.43	97.15	0.78	29.48			
	sd		0.05	0.34	0.50	0.43	0.01	0.17	0.05	NA	0.15	0.22	0.75		3.90			
	cpx	19	0.36	16.14	2.44	53.03	0.27	6.89	0.03	NA	0.43	20.88	100.48	0.81				
	sd		0.21	0.45	0.66	0.71	0.06	0.59	0.01	NA	0.10	0.73	0.71					
	ol	17	b.d.l.	39.98	0.02	39.10	0.41	20.44	0.01	NA	0.03	0.15	100.16	0.78				
	sd		b.d.l.	1.11	0.01	0.73	0.03	1.10	0.01	NA	0.01	0.05	0.90					

This is the peer-reviewed, final accepted version for American Mineralogist, published by the Mineralogical Society of America.
The published version is subject to change. Cite as Authors (Year) Title. American Mineralogist, in press.
DOI: https://doi.org/10.2138/am-2022-8031. http://www.minsocam.org/

ID	Phase	n	Na_2O	MgO	Al_2O_3	SiO_2	MnO	FeO	K_2O	P_2O_5	TiO_2	CaO	Total	Mg#	Fe^{3+}/Fe_{Total}	K_D Fe/Mg ol	K_D Fe/Mg cpx	Anhydrous NBO/T
F137	gl	12	1.89	4.06	19.71	49.76	0.11	4.11	0.75	0.25	0.68	7.19	88.50	0.64	15.62	0.35		0.21
	sd		0.14	0.31	0.34	0.63	0.01	0.14	0.09	0.03	0.03	0.14	0.45					
	am	14	2.38	17.72	12.49	45.21	0.11	6.20	0.33	0.02	1.34	11.43	97.24	0.84	26.37			
	sd		0.08	0.33	0.84	0.80	0.02	0.15	0.01	0.02	0.12	0.10	0.82		3.92			
	ol	15	b.d.l.	44.26	0.03	39.82	0.27	15.53	b.d.l.	0.30	0.03	0.13	100.39	0.84				
	sd		b.d.l.	0.64	0.01	0.43	0.02	0.44	b.d.l.	0.17	0.02	0.03	0.81					
F163	gl	20	1.26	2.67	16.78	52.91	0.15	5.50	1.32	0.66	0.38	5.79	87.37	0.46	16.63	0.26	0.21	0.21
	sd		0.25	0.27	0.38	0.66	0.01	0.18	0.24	0.04	0.02	0.14	0.76					
	am	14	2.13	16.37	11.31	44.83	0.18	9.48	0.76	0.03	1.40	10.93	97.41	0.75	18.16			
	sd		0.05	0.29	0.58	0.62	0.02	0.25	0.09	0.01	0.23	0.23	0.45		6.89			
	cpx	12	0.49	15.79	2.47	53.27	0.23	6.79	0.04	0.05	0.44	20.58	100.15	0.81				
	sd		0.26	0.72	0.99	0.48	0.03	0.59	0.03	0.05	0.09	0.96	0.65					
	ol	13	b.d.l.	39.70	0.02	38.82	0.40	21.25	b.d.l.	0.26	0.02	0.16	100.64	0.77				
	sd		b.d.l.	0.90	0.01	0.38	0.02	0.93	b.d.l.	0.22	0.02	0.06	0.69					
	opx	12	0.02	26.19	2.40	54.06	0.52	15.78	b.d.l.	b.d.l.	0.13	1.44	100.55	0.75				
	sd		0.01	0.29	0.57	0.59	0.02	0.26	b.d.l.	b.d.l.	0.02	0.30	0.49					
F178	am	21	1.90	18.40	10.78	45.71	0.22	7.01	0.82	0.05	0.65	11.68	97.18	0.82	93.33			0.13
	sd		0.08	0.60	0.61	0.58	0.03	0.65	0.06	0.01	0.14	0.38	0.42		2.85			
	gl	17	1.47	1.66	16.45	57.86	0.15	1.79	1.07	0.40	0.22	4.24	86.82	0.62	81.66			
	sd		0.46	0.46	0.34	0.84	0.04	0.13	0.28	0.06	0.05	0.29	4.75					
	tmnt	14	0.00	2.01	1.55	0.01	0.20	79.85	0.02	0.01	6.24	0.13	89.99					
	sd		0.03	0.32	0.11	0.04	0.03	1.43	0.01	0.01	0.94	0.04	0.78					
OD109	gl	15	1.62	3.12	17.30	52.30	0.17	5.44	0.79	0.30	0.49	6.25	87.78	0.51	16.63			0.21
	sd		0.28	0.10	0.30	0.85	0.02	0.09	0.11	0.02	0.04	0.09	1.23					
	am	34	2.27	17.09	11.63	45.48	0.18	8.57	0.29	0.02	1.12	10.94	97.59	0.78	29.34			
	sd		0.06	0.42	0.50	0.73	0.04	0.36	0.03	0.03	0.08	0.38	0.87		2.70			
	opx	11	0.02	28.56	2.47	54.77	0.40	12.71	b.d.l.	b.d.l.	0.15	1.36	100.44	0.80				
	sd		0.01	0.76	0.72	0.65	0.04	0.73	b.d.l.	b.d.l.	0.05	0.14	0.91					
OD138	am	12	1.86	18.86	10.17	47.14	0.24	6.30	0.68	0.05	0.73	11.36	97.34	0.84	91.52			0.23
	sd		0.08	0.48	0.33	0.75	0.03	0.45	0.17	0.04	0.20	0.49	0.41		2.94			
	gl	23	1.11	1.15	16.22	61.54	0.11	1.31	0.83	0.28	0.19	3.81	86.52	0.61	81.66			
	sd		0.22	0.60	0.31	0.69	0.03	0.17	0.16	0.06	0.05	0.43	1.35					
	tmnt	15	0.07	2.08	1.83	0.65	0.21	78.59	0.03	b.d.l.	5.76	0.27	89.44	0.04				
	sd		0.11	0.36	0.37	1.10	0.03	1.18	0.03	b.d.l.	0.27	0.12	0.82					
	phos	3	0.03	0.56	0.06	0.23	0.15	0.10	0.04	41.82	b.d.l.	54.46	97.53					
	sd		0.01	0.05	0.04	0.06	0.02	0.02	0.01	0.22	b.d.l.	2.09	1.98					

This is the peer-reviewed, final accepted version for American Mineralogist, published by the Mineralogical Society of America.
The published version is subject to change. Cite as Authors (Year) Title. American Mineralogist, in press.
DOI: https://doi.org/10.2138/am-2022-8031. http://www.minsocam.org/

ID	Phase	n	Na_2O	MgO	Al_2O_3	SiO_2	MnO	FeO	K_2O	P_2O_5	TiO_2	CaO	Total	Mg#	Fe^{3+}/Fe_{Total}	K_D Fe/Mg ol	K_D Fe/Mg cpx	Anhydrous NBO/T
F174	am	17	1.80	15.76	10.82	46.24	0.22	10.46	0.63	0.06	1.16	10.73	97.85	0.73	30.15			0.26
	sd		0.09	0.66	0.42	0.49	0.02	0.37	0.10	0.03	0.08	0.34	0.48		4.31			
	gl	16	1.29	1.42	17.29	57.72	0.15	4.07	0.78	0.46	0.28	4.46	87.87	0.38	20.12			
	sd		0.16	0.22	0.19	0.51	0.03	0.40	0.06	0.10	0.06	0.18	0.67					
	opx	15	0.02	24.70	2.05	54.39	0.53	17.38	0.03	b.d.l.	0.14	1.40	100.63	0.72				
	sd		0.01	0.64	0.41	0.46	0.02	0.58	0.01	b.d.l.	0.02	0.13	0.37					
	phos	5	0.02	0.46	0.18	1.02	0.10	0.68	0.08	41.20	0.02	54.84	98.57					
	sd		0.01	0.12	1.45	0.02	0.05	0.03	1.61	0.02	0.27	0.51						
F177	gl	20	1.80	1.88	16.42	56.72	0.19	6.17	0.55	NA	0.59	6.11	90.36	0.35	19.40			0.15
	sd		0.04	0.02	0.06	0.53	0.01	0.08	0.02	NA	0.04	0.07	0.58					
	plag	14	1.54	0.08	35.04	46.49	0.01	0.67	0.02	NA	0.03	17.56	101.44					
	sd		0.39	0.05	0.84	0.96	0.01	0.18	0.01	NA	0.02	0.57	0.34					
	am	21	1.85	14.19	11.64	44.16	0.31	13.15	0.13	NA	1.63	10.68	97.72	0.66	21.46			
	sd		0.05	0.48	0.52	0.53	0.02	0.64	0.01	NA	0.12	0.23	0.33		6.71			
	opx	14	b.d.l.	21.65	2.12	52.54	0.77	21.54	b.d.l.	NA	0.21	1.72	100.53	0.64				
	sd		b.d.l.	0.45	0.74	0.74	0.02	0.33	b.d.l.	NA	0.04	0.16	0.43					
F179	am	8	0.84	18.24	10.31	48.25	0.27	6.96	0.36	0.06	0.66	11.59	97.49	0.82	85.12			0.07
	sd		0.06	1.33	0.88	1.04	0.03	1.38	0.05	0.02	0.29	0.46	0.82		3.66			
	gl	17	0.75	2.51	16.05	58.09	0.15	1.67	0.59	0.51	0.20	5.82	86.29	0.73	84.27			
	sd		0.11	0.16	0.20	1.02	0.05	0.20	0.04	0.11	0.05	0.16	1.26					
	tmnt	10	b.d.l.	1.10	2.05	0.07	0.10	82.76	0.01	0.01	4.04	0.16	90.26					
	sd		b.d.l.	0.35	0.29	0.04	0.02	1.50	0.01	0.01	0.80	0.07	0.39					
OD129	gl	20	1.18	1.65	17.05	53.73	0.18	5.48	0.54	NA	0.48	6.30	86.53	0.35	17.16			0.16
	sd		0.06	0.05	0.10	0.22	0.01	0.11	0.01	NA	0.02	0.06	0.35					
	am	18	2.03	13.02	13.09	43.16	0.30	13.69	0.21	NA	1.39	10.64	97.51	0.63	14.42			
	sd		0.03	0.26	0.29	0.24	0.02	0.26	0.02	NA	0.09	0.15	0.41		2.71			
F176	gl	19	1.52	1.37	16.42	56.78	0.19	5.29	0.54	NA	0.44	5.83	88.31	0.32	20.49			0.10
	sd		0.05	0.02	0.05	0.31	0.01	0.04	0.01	NA	0.02	0.05	0.40					
	am	18	1.81	12.53	11.78	44.04	0.37	14.89	0.16	NA	1.63	10.72	97.92	0.60	20.42			
	sd		0.07	0.94	0.69	0.71	0.05	1.02	0.02	NA	0.11	0.33	0.17		4.76			
	plag	13	1.26	0.07	35.22	46.25	0.02	0.69	0.03	NA	0.03	17.78	101.32					
	sd		0.12	0.05	0.89	0.60	0.01	0.29	0.02	NA	0.03	0.47	0.87					
MC69	gl	11	4.57	0.72	16.06	61.35	0.03	2.08	1.08	NA	0.34	4.21	90.44	0.38	31.59			0.05
	sd		0.28	0.18	0.15	0.53	0.03	0.27	0.08	NA	0.05	0.15	0.52					
	am	7	1.87	16.11	10.69	46.39	0.10	9.54	0.20	NA	1.68	11.22	97.84	0.75	21.38			
	sd		0.18	0.82	0.71	1.12	0.05	1.04	0.04	NA	0.15	0.23	0.72		6.22			

This is the peer-reviewed, final accepted version for American Mineralogist, published by the Mineralogical Society of America.
The published version is subject to change. Cite as Authors (Year) Title. American Mineralogist, in press.
DOI: https://doi.org/10.2138/am-2022-8031. http://www.minsocam.org/

ID	Phase	n	Na_2O	MgO	Al_2O_3	SiO_2	MnO	FeO	K_2O	P_2O_5	TiO_2	CaO	Total	Mg#	Fe^{3+}/Fe_{Total}	K_D Fe/Mg ol	K_D Fe/Mg cpx	Anhydrous NBO/T
OD131	gl	14	1.15	1.12	17.23	53.32	0.17	4.30	0.53	NA	0.34	5.96	84.07	0.32	18.11			0.17
	sd		0.07	0.06	0.11	0.47	0.02	0.12	0.04	NA	0.01	0.06	0.59					
	am	17	1.98	10.73	14.93	41.32	0.36	15.85	0.24	NA	1.29	10.37	97.05	0.55	16.72			
	sd		0.06	0.57	0.55	0.68	0.03	0.54	0.03	NA	0.17	0.30	0.37		1.26			
OD139	gl	18	0.83	1.93	16.07	59.32	0.18	1.04	0.43	NA	0.16	6.53	86.45	0.77	86.28			0.04
	sd		0.03	0.03	0.06	0.58	0.01	0.04	0.02	NA	0.02	0.04	0.59					
	plag	7	0.61	0.08	38.96	42.91	0.02	0.47	0.02	NA	0.02	17.94	101.01					
	sd		0.12	0.03	3.78	1.91	0.01	0.02	0.01	NA	0.01	1.02	1.60					
	tmnt	10	0.02	1.19	2.07	0.07	0.22	80.84	b.d.l.	NA	4.42	0.16	88.98					
	sd		0.02	0.41	0.17	0.10	0.06	1.59	b.d.l.	NA	1.26	0.04	0.71					
	am	14	0.70	18.49	10.92	48.72	0.47	5.42	0.11	NA	0.46	12.11	97.38	0.86	90.91			
	sd		0.06	0.45	0.86	0.83	0.03	0.31	0.01	NA	0.11	0.16	0.43		3.30			
MC48	gl	9	4.68	0.78	14.62	65.26	0.07	2.56	1.45	NA	0.39	2.92	92.71	0.35	33.21			0.05
	sd		0.18	0.02	0.14	0.56	0.03	0.16	0.04	NA	0.04	0.09	0.72					
	am	10	1.79	15.69	11.74	45.63	0.15	10.99	0.16	NA	10.65	1.41	98.23	0.72	17.40			
	sd		0.09	0.57	0.56	0.80	0.03	0.62	0.02	NA	0.32	0.27	0.57		2.50			
MC49	gl	11	4.72	0.47	13.65	66.98	0.08	1.67	1.60	NA	0.25	2.17	91.59	0.34	34.17			0.03
	sd		0.20	0.02	0.22	0.66	0.05	0.12	0.06	NA	0.03	0.08	0.98					
	am	10	1.77	15.91	11.17	46.26	0.15	10.43	0.17	NA	10.41	1.53	97.80	0.73	23.83			
	sd		0.12	0.66	0.91	0.77	0.06	0.59	0.04	NA	0.67	0.28	0.31		7.86			
MC68	gl	13	4.50	0.75	15.31	62.51	0.06	2.22	1.33	NA	0.30	3.20	90.18	0.38	33.39			0.04
	sd		0.22	0.05	0.19	0.47	0.03	0.17	0.05	NA	0.03	0.08	0.58					
	am	16	1.90	15.08	10.30	45.72	0.13	11.54	0.21	NA	1.75	10.99	97.65	0.70	23.82			
	sd		0.18	0.57	0.97	1.20	0.04	0.69	0.04	NA	0.20	0.37	0.73		4.66			
MC51	gl	7	4.56	0.49	13.40	68.18	0.04	1.28	1.77	NA	0.26	1.74	91.72	0.40	35.22			0.02
	sd		0.24	0.03	0.13	0.56	0.04	0.10	0.04	NA	0.05	0.11	0.54					
	am	6	1.91	15.58	11.70	45.35	0.13	11.16	0.20	NA	10.59	1.49	98.11	0.71	32.26			
	sd		0.13	0.71	1.02	0.74	0.04	0.71	0.03	NA	0.73	0.20	0.58		6.15			

This is the peer-reviewed, final accepted version for American Mineralogist, published by the Mineralogical Society of America.
The published version is subject to change. Cite as Authors (Year) Title. American Mineralogist, in press.
DOI: https://doi.org/10.2138/am-2022-8031. http://www.minsocam.org/

Table 4. Average amphibole Fe^{3+}/Fe^{2+}, glass Fe^{3+}/Fe^{2+}, and partition coefficients for each experiment with 1 sigma uncertainty. Uncertainty was propagated analytically through the calculation of the partition coefficients for each experiment using the uncertainty of the DEVAS calibration and the standard deviation of average compositions for glass and amphibole from EPMA .

ID	f_{O2}	Amph Fe^{3+}/Fe^{2+}	Glass Fe^{3+}/Fe^{2+}	DFe^{3+}	Sigma DFe^{3+}	DFe^{2+}	Sigma DFe^{2+}	DMg	KFe^{2+}/Mg	Sigma KFe^{2+}/Mg	KFe^{3+}/Fe^{2+}	Sigma KFe^{3+}/Fe^{2+}
OD143	NNO	0.47	0.19	2.29	0.77	0.95	0.15	3.86	0.25	0.04	2.41	0.90
OD144	NNO	0.47	0.19	2.64	0.89	1.06	0.17	4.43	0.24	0.04	2.49	0.93
OD102	NNO	0.44	0.19	2.33	0.83	1.01	0.16	3.95	0.26	0.04	2.30	0.89
F136	NNO	0.42	0.20	2.31	0.84	1.09	0.17	5.01	0.22	0.04	2.12	0.84
F137	NNO	0.36	0.19	2.05	0.84	1.06	0.16	3.53	0.30	0.05	1.93	0.84
F163	NNO	0.22	0.20	1.51	0.90	1.36	0.18	4.94	0.28	0.05	1.11	0.68
F178	RuRuO2	14.00	4.45	3.46	0.40	1.10	1.78	8.77	0.13	0.22	3.15	5.11
OD109	NNO	0.42	0.20	2.22	0.82	1.07	0.16	4.43	0.24	0.04	2.08	0.83
OD138	RuRuO2	10.79	4.45	4.25	0.50	1.75	2.23	13.06	0.13	0.30	2.42	3.10
F174	NNO	0.43	0.25	3.10	1.11	1.81	0.28	8.99	0.20	0.06	1.71	0.67
F177	NNO	0.27	0.24	2.04	1.02	1.79	0.25	6.35	0.28	0.07	1.14	0.59
F179	RuRuO2	5.72	5.36	3.44	0.44	3.22	2.34	5.72	0.56	1.32	1.07	0.79
OD129	NNO	0.17	0.21	1.71	1.28	2.11	0.27	6.45	0.33	0.09	0.81	0.62
F176	NNO	0.26	0.26	2.35	1.24	2.36	0.32	7.67	0.31	0.10	1.00	0.54
MC69	NNO+1	0.27	0.46	2.58	1.30	4.38	0.60	18.29	0.24	0.14	0.59	0.31
OD131	NNO	0.20	0.22	2.80	1.81	3.08	0.40	7.84	0.39	0.16	0.91	0.60
OD139	RuRuO2	10.00	6.29	4.39	0.52	2.76	3.28	7.67	0.36	1.18	1.59	1.90
MC48	NNO+1	0.21	0.50	1.91	1.19	4.52	0.59	17.05	0.26	0.16	0.42	0.27
MC49	NNO+1	0.31	0.52	3.68	1.67	6.10	0.87	28.52	0.21	0.19	0.60	0.29
MC68	NNO+1	0.31	0.50	3.09	1.40	4.96	0.70	16.71	0.30	0.21	0.62	0.30
MC51	NNO+1	0.48	0.54	6.74	2.26	7.70	1.23	27.61	0.28	0.34	0.88	0.32

This is the peer-reviewed, final accepted version for American Mineralogist, published by the Mineralogical Society of America.
The published version is subject to change. Cite as Authors (Year) Title. American Mineralogist, in press.
DOI: https://doi.org/10.2138/am-2022-8031. http://www.minsocam.org/

Table 5. Mean and 2 standard error (SE) of DFe^{3+}, DFe^{2+}, DMg, KFe^{2+}/Mg, and KFe^{3+}/Fe^{2+} for all intermediate f_{O2} experiments (i.e., experiments conducted at NNO and NNO+1), high f_{O2} experiments (i.e., experiments conducted at Ru-RuO_2), and intermediate f_{O2} experiments with basalt, andesite, or dacite starting compositions separately. 2SE is calculated by dividing the standard deviation of the average for each group by the square root of the number of experiments in that group, and then multiplying that quantity by two.

Starting Composition	Oxygen Fugacity	No. Experiments	DFe^{3+}	2SE	DFe^{2+}	2SE	DMg	2SE	KFe^{2+}/Mg	2SE	KFe^{3+}/Fe^{2+}	2SE
All	Intermediate	17	2.66	0.57	2.73	1.00	10.33	3.99	0.27	0.02	1.36	0.35
All	Ru-RuO_2	4	3.88	0.51	2.21	0.96	8.80	3.10	0.30	0.21	2.06	0.92
Basalt	Intermediate	8	2.30	0.32	1.18	0.20	4.89	1.22	0.25	0.03	2.02	0.31
Andesite	Intermediate	4	2.22	0.46	2.34	0.55	7.08	0.79	0.33	0.05	0.96	0.14
Dacite	Intermediate	5	3.60	1.67	5.53	1.24	21.64	5.28	0.26	0.03	0.62	0.15

This is the peer-reviewed, final accepted version for American Mineralogist, published by the Mineralogical Society of America.
The published version is subject to change. Cite as Authors (Year) Title. American Mineralogist, in press.
DOI: https://doi.org/10.2138/am-2022-8031. http://www.minsocam.org/

Table 6. Mean amphibole Fe^{3+}/Fe^{2+}, calculated f_{O2}, percent dehydrogenation, and residence times in andesite for samples from Shiveluch. Uncertainty in f_{O2} was calculated using a Monte Carlo appraoch, repeating the calculation 10,000 times with values normally distributed around the standard deviations of the amphibole Fe^{3+}/Fe^{2+} and the standard error of KFe^{3+}/Fe^{2+} for intermediate basalts (see Table 5). The median and interquartile range of residence times were calculated using a similar approach, repeating the calculation 10,000 times with starting values normally distributed around the mean and 2SE of amphibole FeO and Fe^{3+}/Fe_{Total} in the sample.

Sample	No. Points	Average Amphibole Fe^{3+}/Fe_{total}	SD Amphibole Fe^{3+}/Fe_{Total}	Average Amphibole Fe^{3+}/Fe^{2+}	SD Amphibole Fe^{3+}/Fe^{2+}	f_{O2} (ΔNNO)	SD f_{O2}	SE f_{O2}	Percent dehydrogenation	Median Time (days)	Median Time (months)	IQR (days)
16b	48	35.10	7.66	0.56	0.20	1.87	0.96	0.14				
3600 Tephra	37	38.11	5.94	0.62	0.21	2.20	0.64	0.10				
09a	19	40.68	5.51	0.69	0.22	2.44	0.58	0.13	6.54	6	0.20	7.5
02b	21	42.34	5.96	0.75	0.24	2.62	0.65	0.14	8.41	11	0.25	11
06a	23	43.78	3.54	0.78	0.24	2.80	0.37	0.07	9.32	13	0.42	6.3
04l	29	46.30	4.51	0.87	0.27	2.99	0.46	0.08				
15f	31	47.54	7.26	0.93	0.29	3.06	0.72	0.13	14.3	31	1.0	19
5	24	51.14	6.54	1.07	0.33	3.47	0.67	0.14	20.4	64	2.1	35
04d	33	53.50	6.01	1.17	0.36	3.50	0.71	0.12	20.8	68	2.2	29
04b	40	53.79	6.22	1.19	0.37	3.58	0.67	0.10	21.0	69	2.3	26
04k	46	59.08	10.2	1.58	0.51	3.98	1.38	0.20	25.2	102	3.4	52

This is the peer-reviewed, final accepted version for American Mineralogist, published by the Mineralogical Society of America.
The published version is subject to change. Cite as Authors (Year) Title. American Mineralogist, in press.
DOI: https://doi.org/10.2138/am-2022-8031. http://www.minsocam.org/

Figure 1

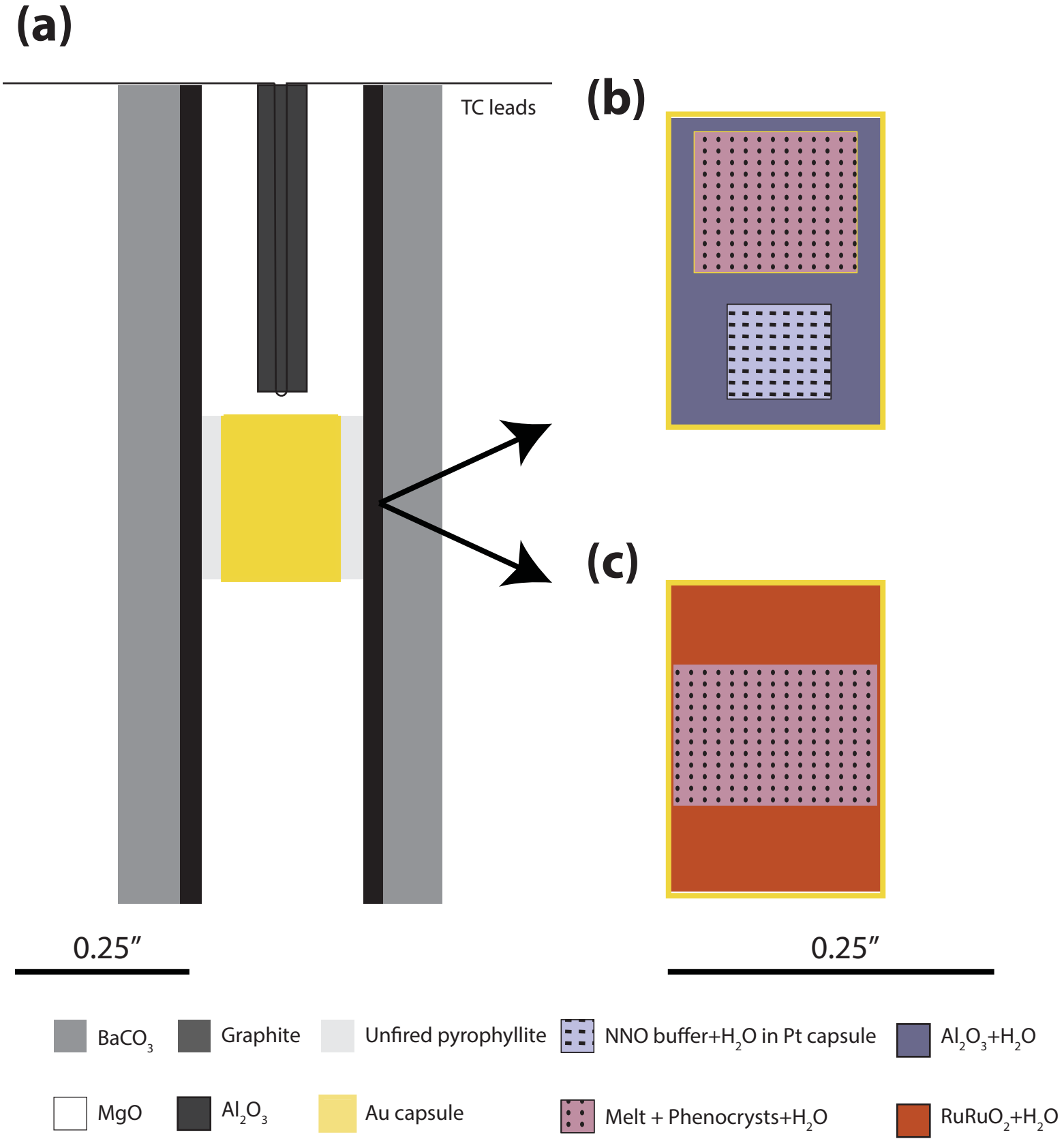

This is the peer-reviewed, final accepted version for American Mineralogist, published by the Mineralogical Society of America.
The published version is subject to change. Cite as Authors (Year) Title. American Mineralogist, in press.
DOI: https://doi.org/10.2138/am-2022-8031. http://www.minsocam.org/

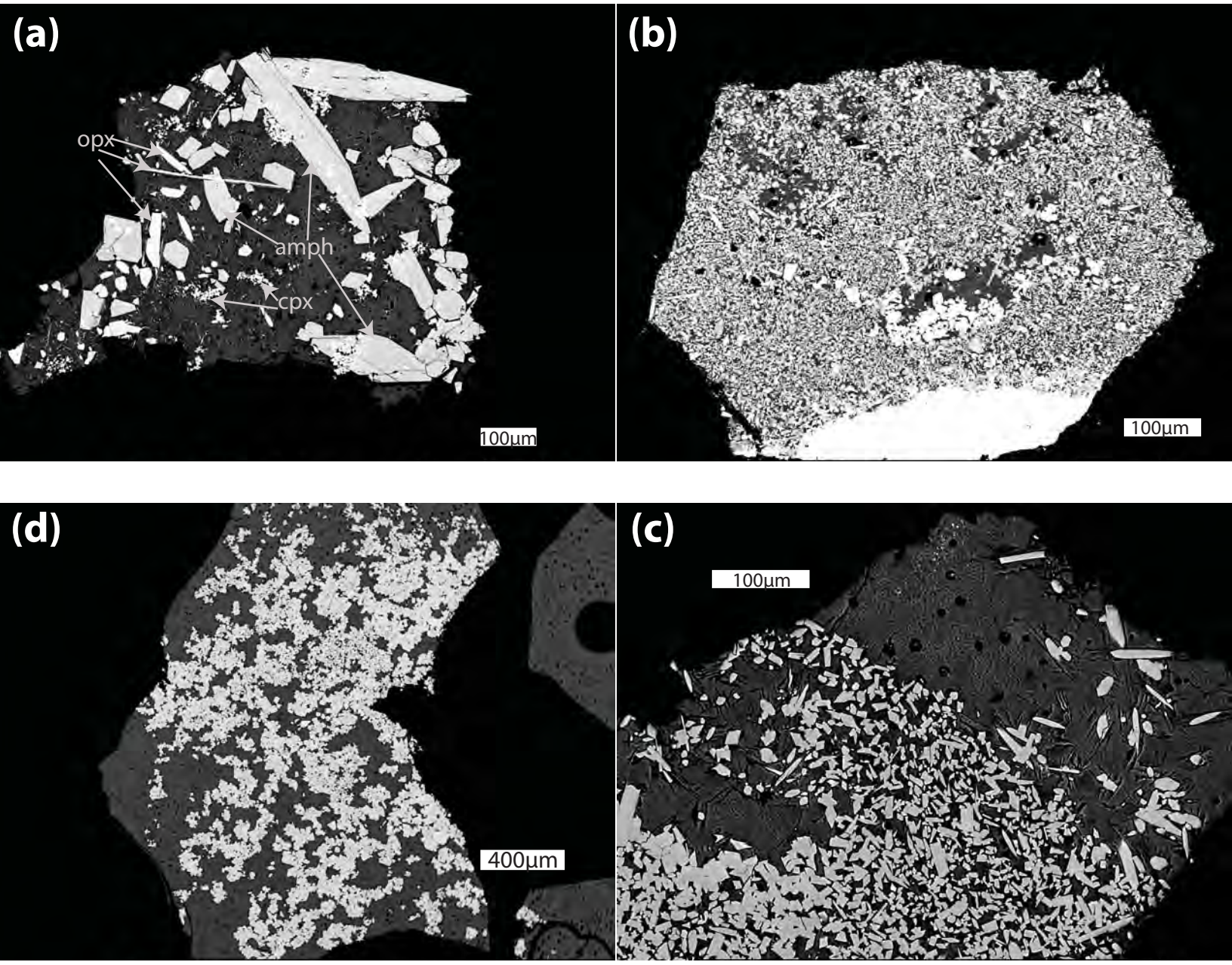

Figure 2

This is the peer-reviewed, final accepted version for American Mineralogist, published by the Mineralogical Society of America.
The published version is subject to change. Cite as Authors (Year) Title. American Mineralogist, in press.
DOI: https://doi.org/10.2138/am-2022-8031. http://www.minsocam.org/

Figure 3

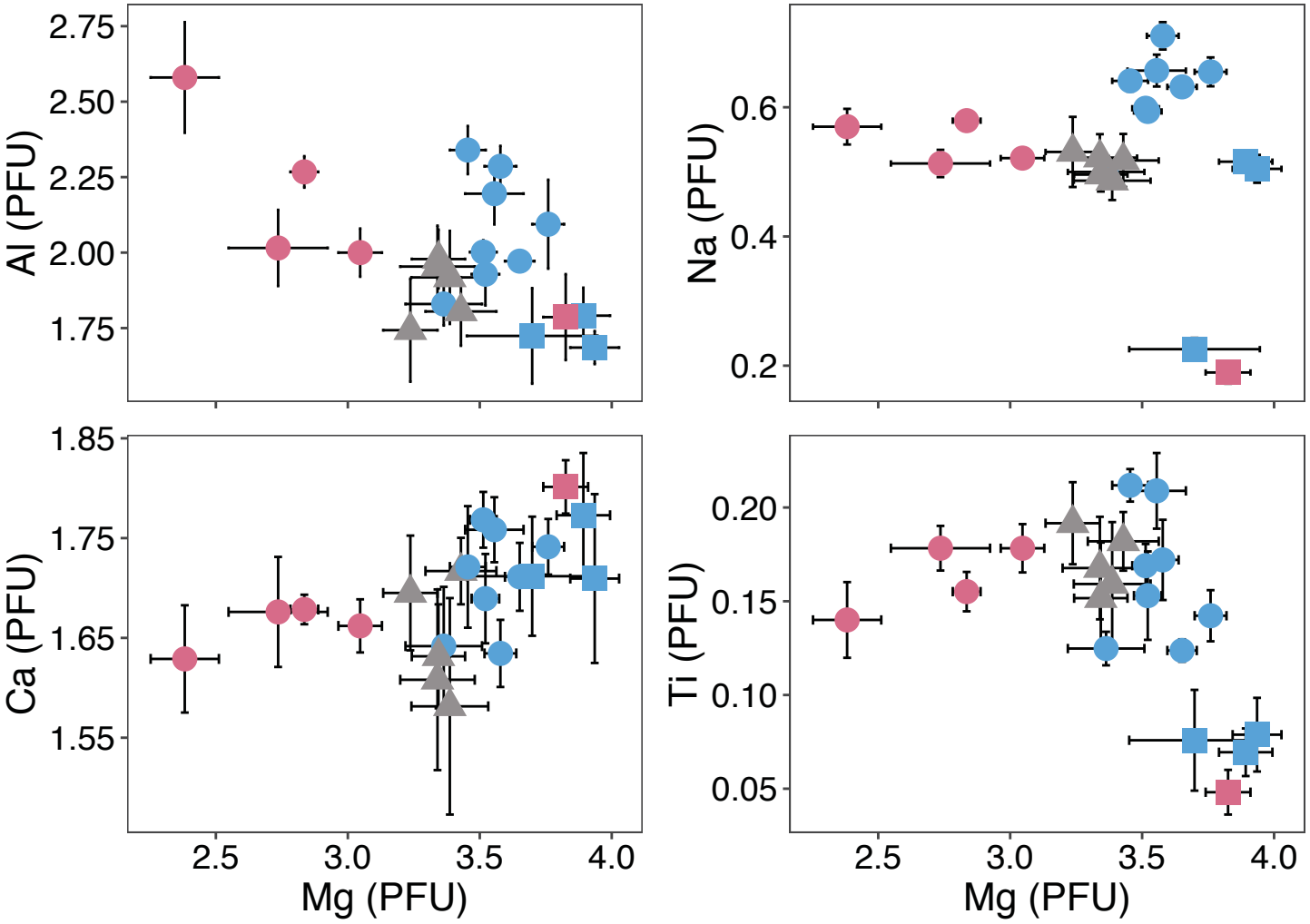

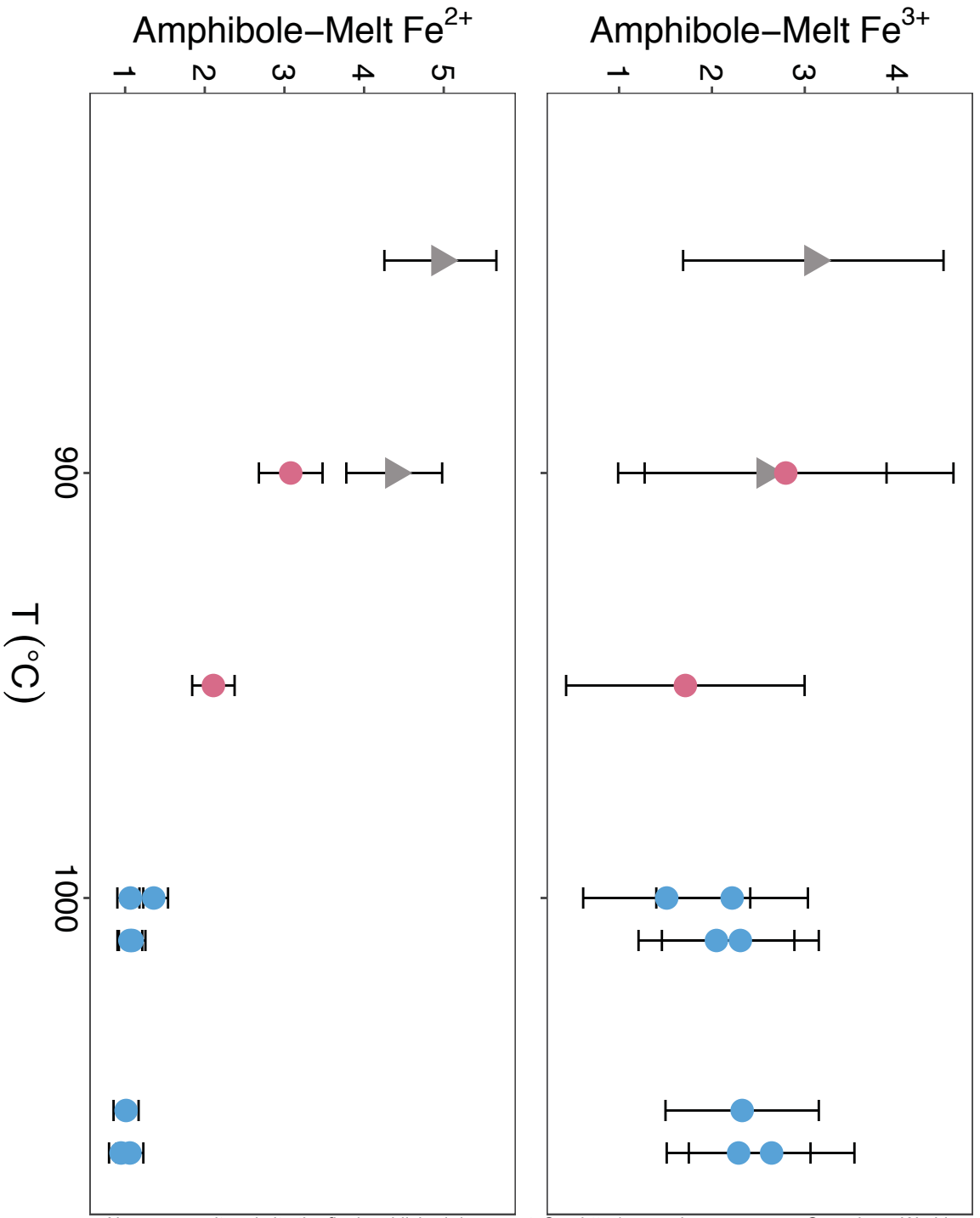

Figure 4

This is the peer-reviewed, final accepted version for American Mineralogist, published by the Mineralogical Society of America.
The published version is subject to change. Cite as Authors (Year) Title. American Mineralogist, in press.
DOI: https://doi.org/10.2138/am-2022-8031. http://www.minsocam.org/

Figure 5

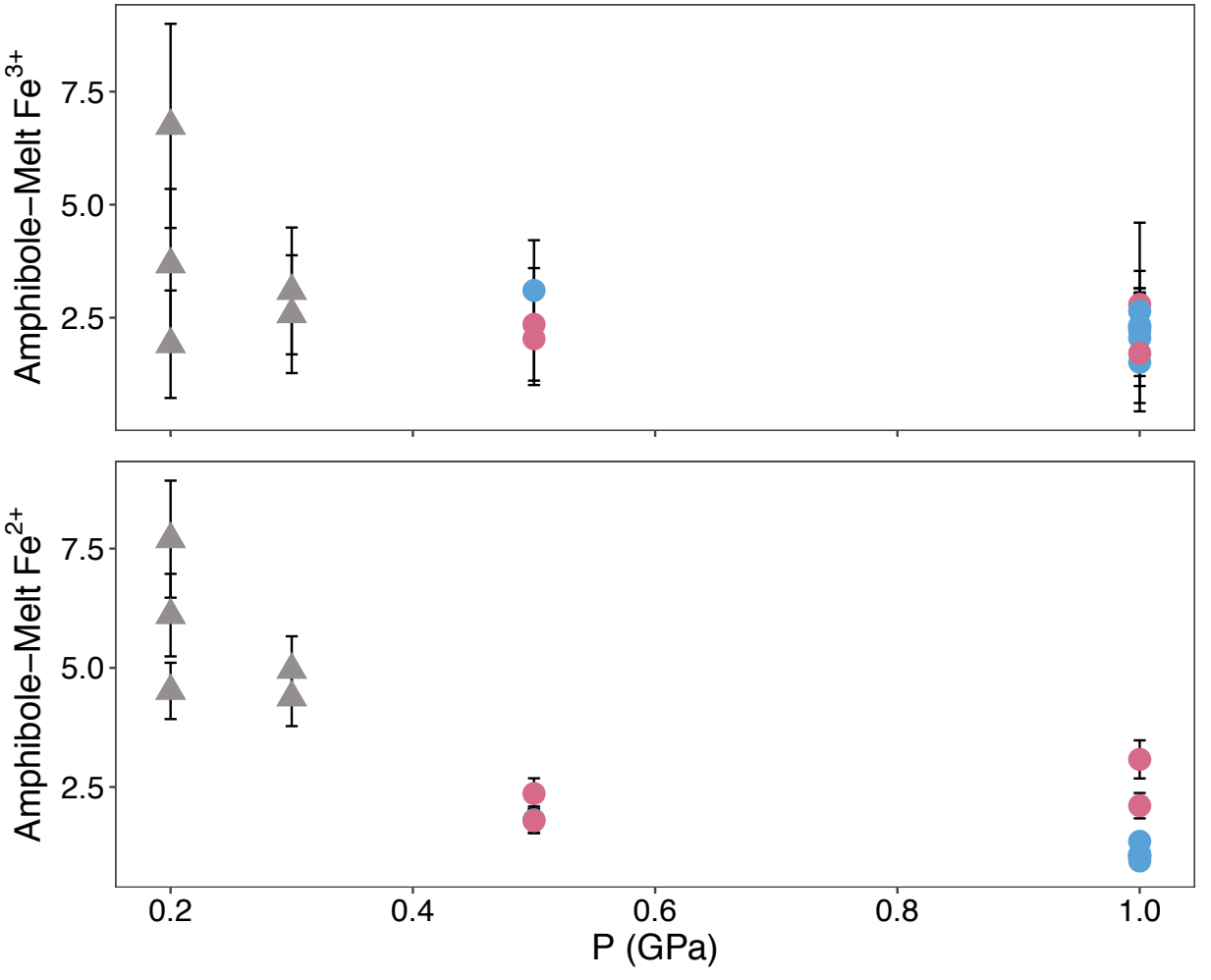

This is the peer-reviewed, final accepted version for American Mineralogist, published by the Mineralogical Society of America.
The published version is subject to change. Cite as Authors (Year) Title. American Mineralogist, in press.
DOI: https://doi.org/10.2138/am-2022-8031. http://www.minsocam.org/

Figure 6

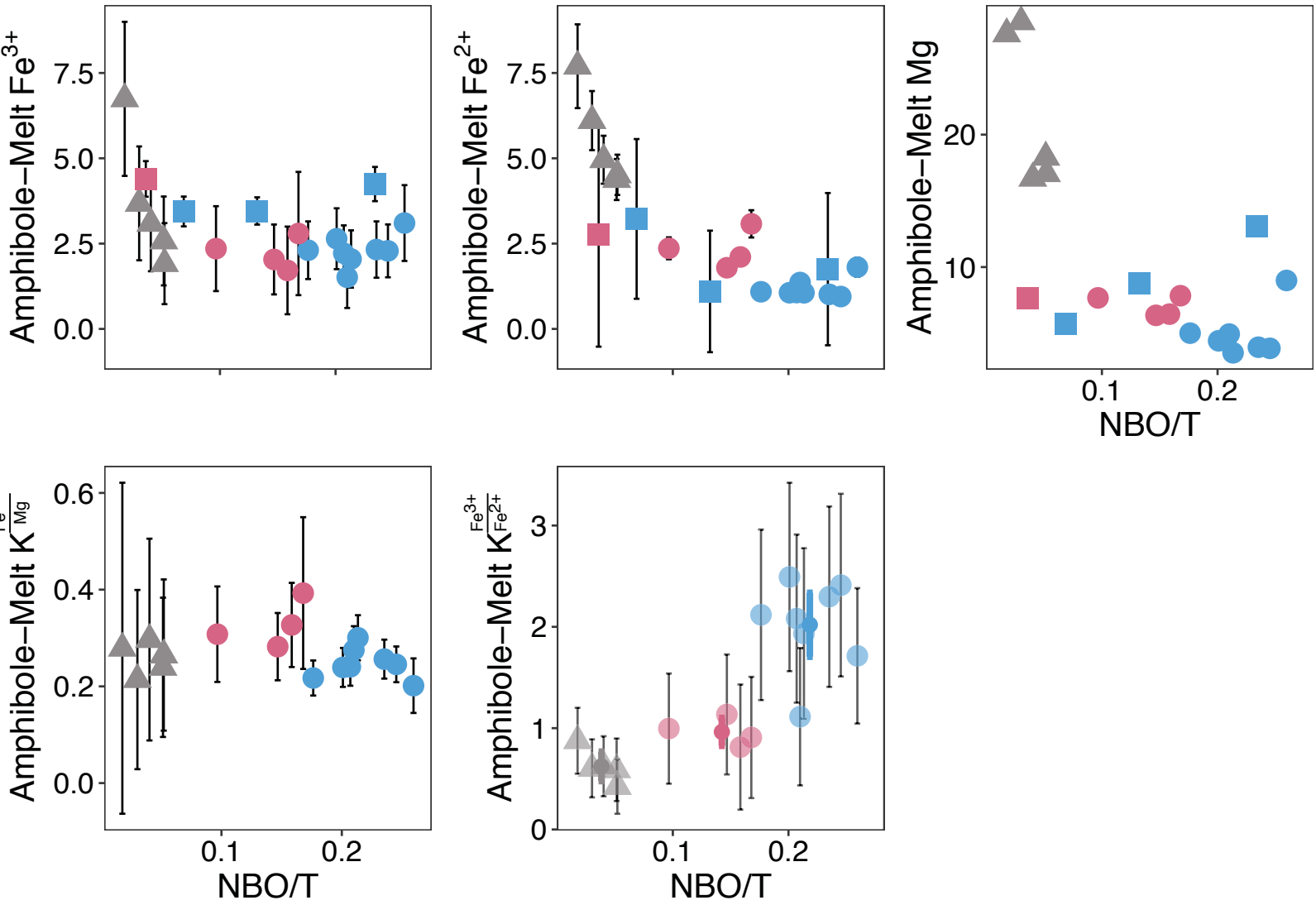

This is the peer-reviewed, final accepted version for American Mineralogist, published by the Mineralogical Society of America.
The published version is subject to change. Cite as Authors (Year) Title. American Mineralogist, in press.
DOI: https://doi.org/10.2138/am-2022-8031. http://www.minsocam.org/

Figure 7

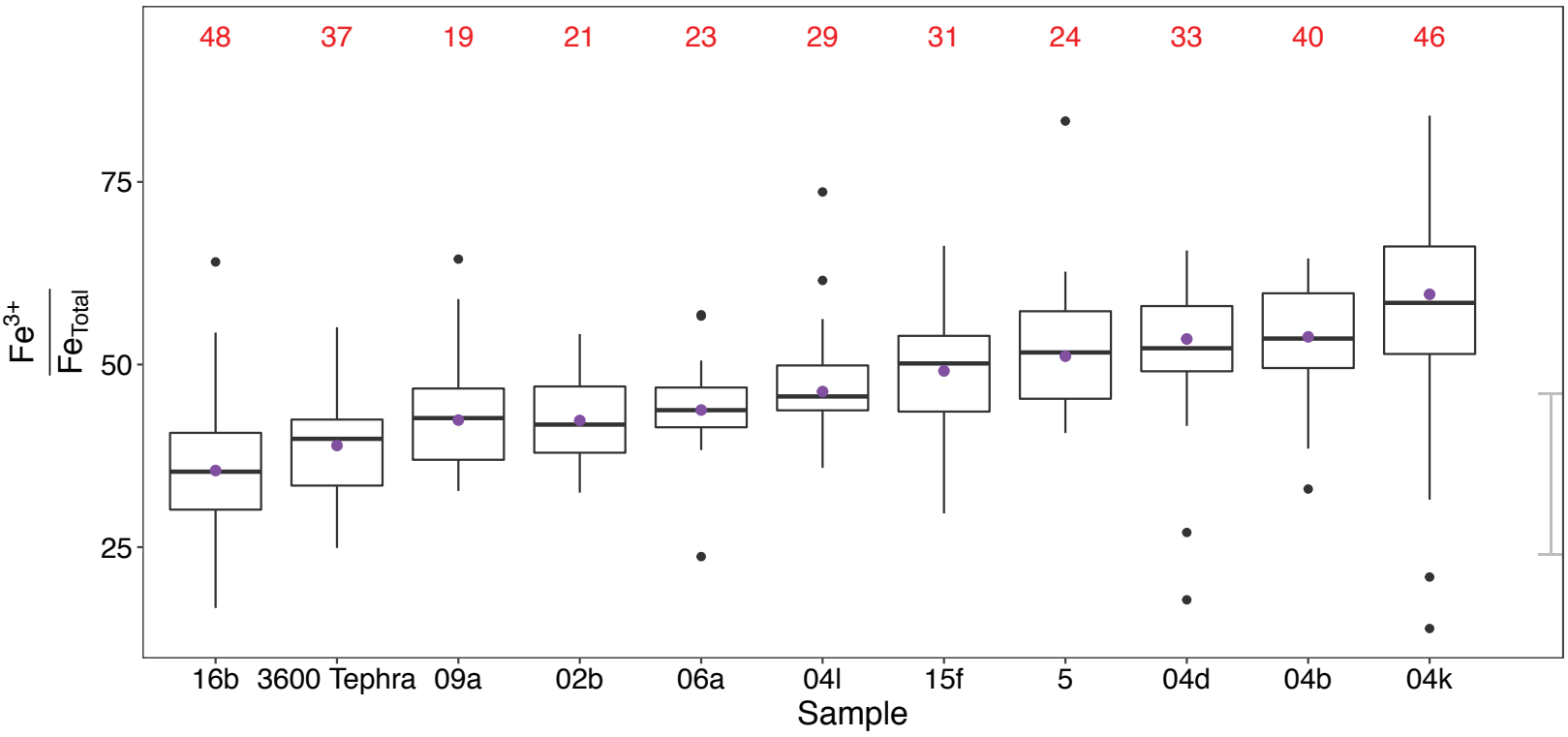

This is the peer-reviewed, final accepted version for American Mineralogist, published by the Mineralogical Society of America.
The published version is subject to change. Cite as Authors (Year) Title. American Mineralogist, in press.
DOI: https://doi.org/10.2138/am-2022-8031. http://www.minsocam.org/

Figure 8

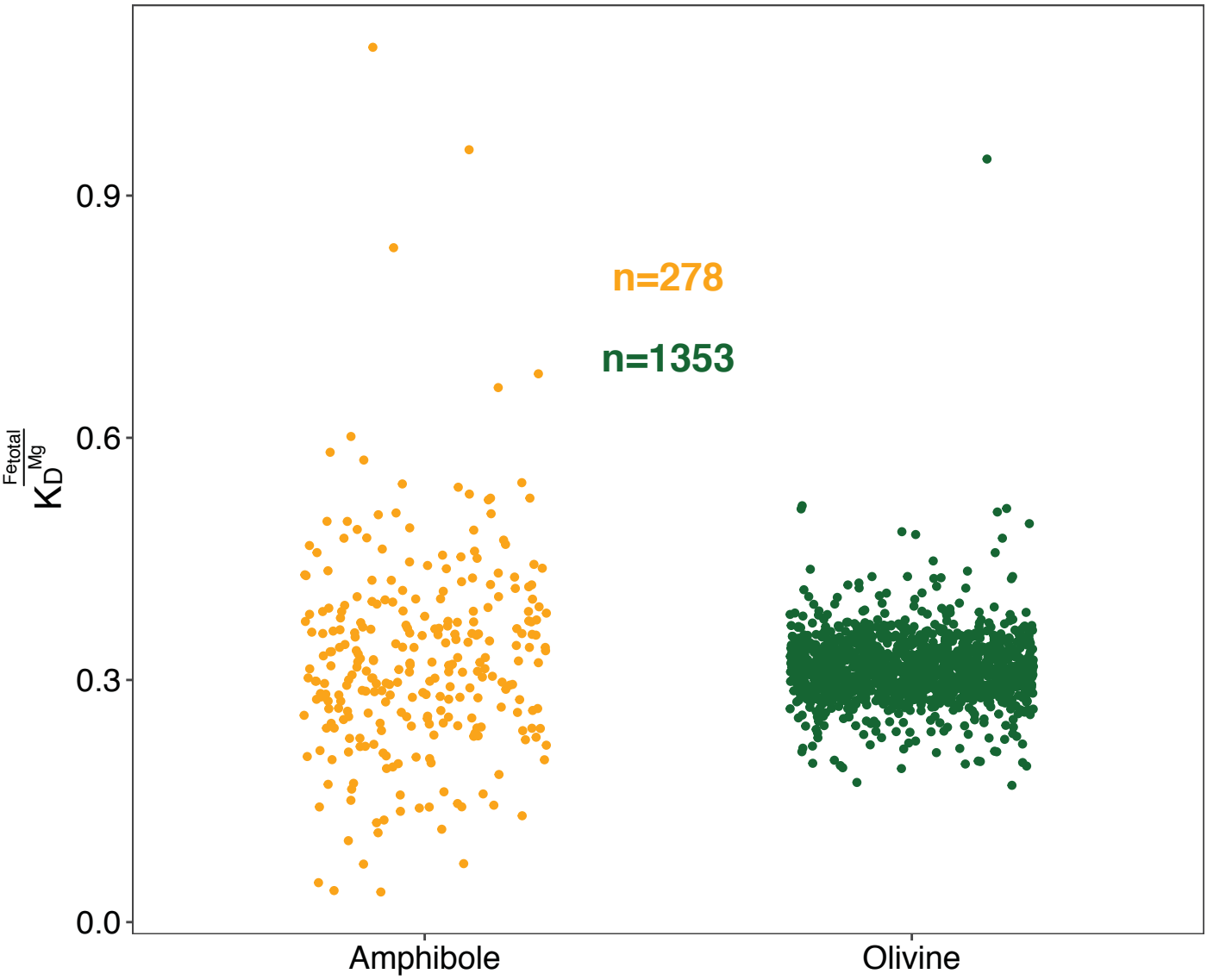

This is the peer-reviewed, final accepted version for American Mineralogist, published by the Mineralogical Society of America.
The published version is subject to change. Cite as Authors (Year) Title. American Mineralogist, in press.
DOI: https://doi.org/10.2138/am-2022-8031. http://www.minsocam.org/

Figure 9

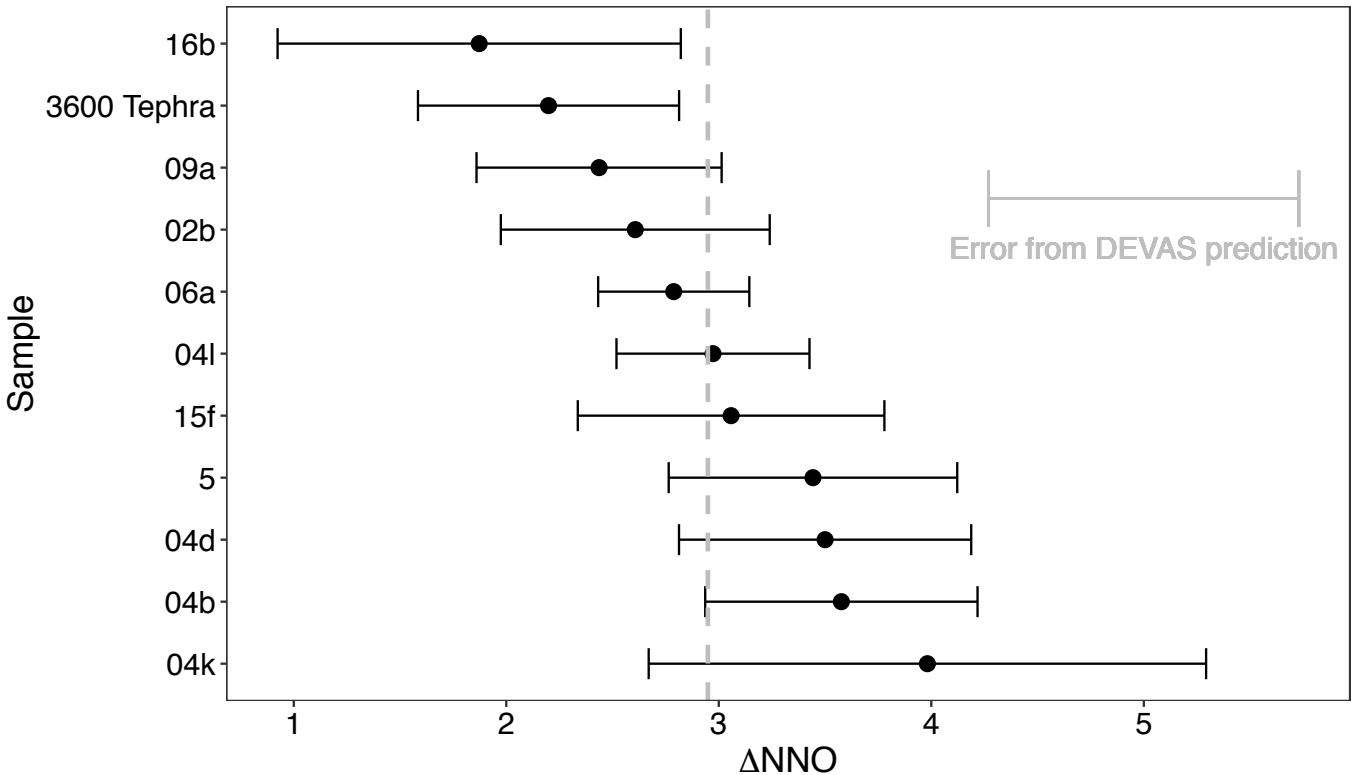

This is the peer-reviewed, final accepted version for American Mineralogist, published by the Mineralogical Society of America.
The published version is subject to change. Cite as Authors (Year) Title. American Mineralogist, in press.
DOI: https://doi.org/10.2138/am-2022-8031. http://www.minsocam.org/

Figure 10

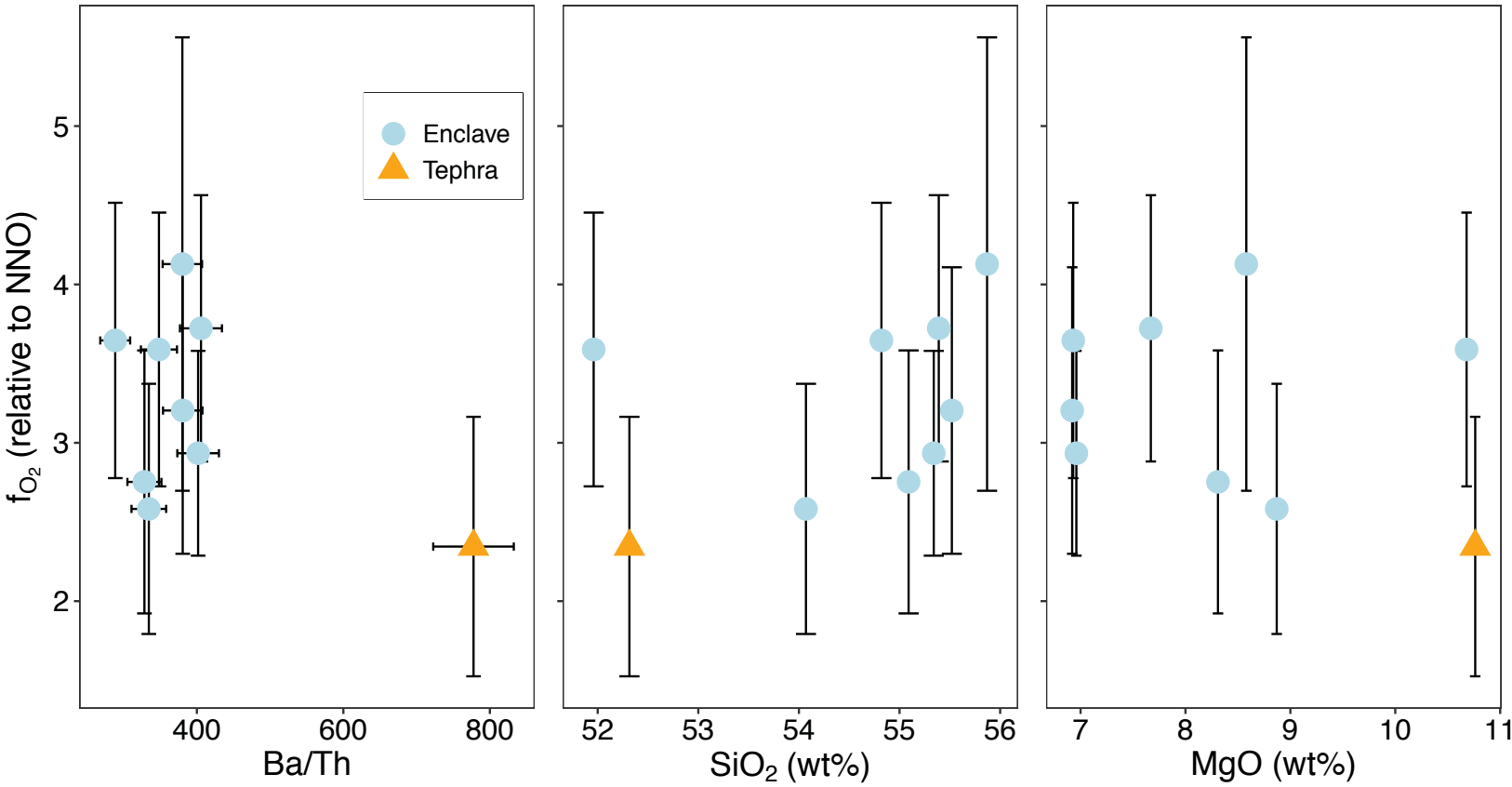

This is the peer-reviewed, final accepted version for American Mineralogist, published by the Mineralogical Society of America.
The published version is subject to change. Cite as Authors (Year) Title. American Mineralogist, in press.
DOI: https://doi.org/10.2138/am-2022-8031. http://www.minsocam.org/

Figure 11

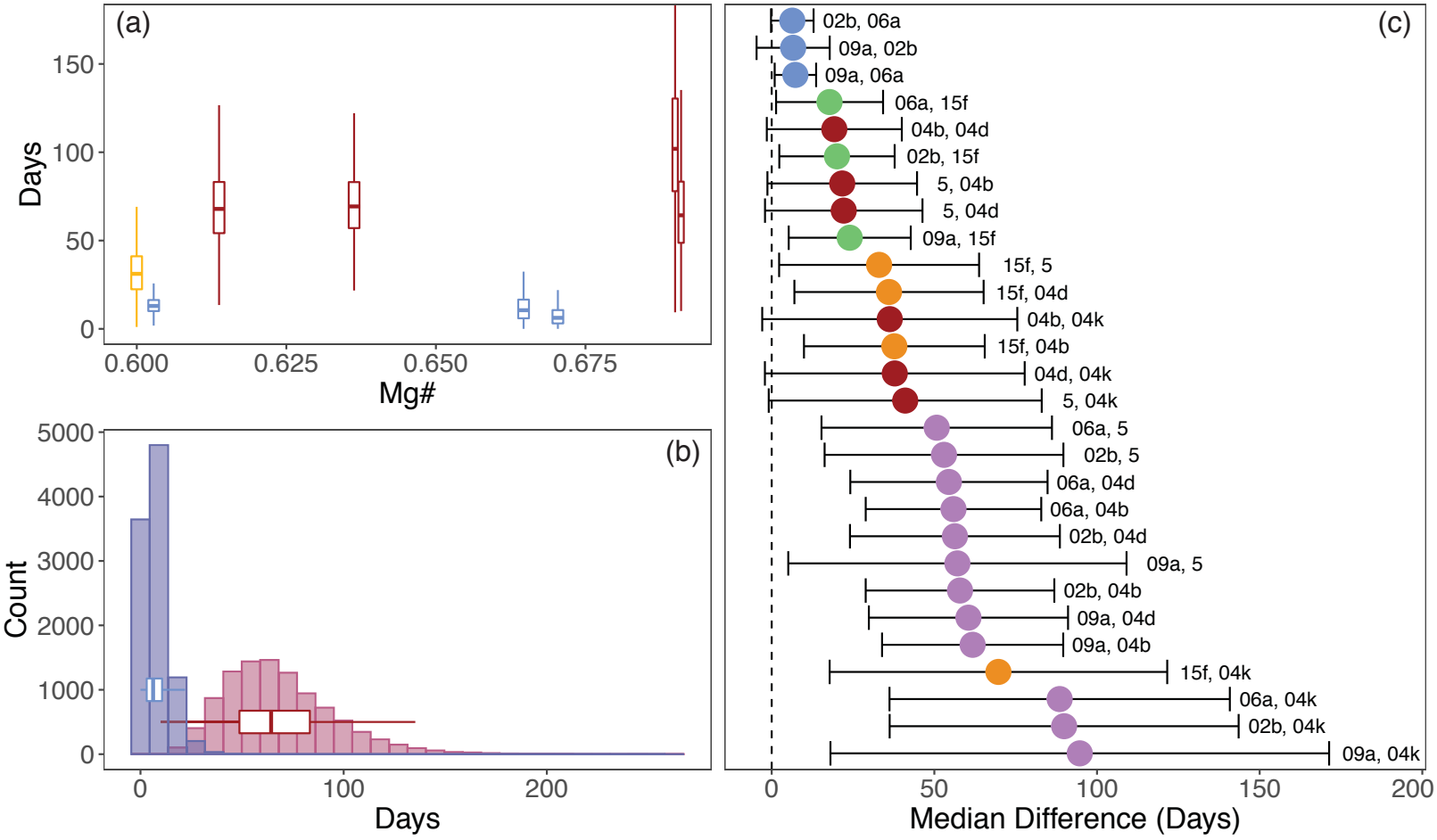

This is the peer-reviewed, final accepted version for American Mineralogist, published by the Mineralogical Society of America.
The published version is subject to change. Cite as Authors (Year) Title. American Mineralogist, in press.
DOI: https://doi.org/10.2138/am-2022-8031. http://www.minsocam.org/

Figure 12